Ultrasonics 128 (2023) 106880

Contents lists available at ScienceDirect

Ultrasonics

journal homepage: www.elsevier.com/locate/ultras

Inverse modeling and experimental validation for reconstructing wave sources on a 2D solid from surficial measurement

Stephen Lloyd [a], Christoph Schaal [b,c], Chanseok Jeong [a,d,*]

[a] School of Engineering and Technology, Central Michigan University, Mount Pleasant, 48859, MI, USA
[b] Department of Mechanical Engineering, California State University, Northridge, 91330, CA, USA
[c] Mechanical and Aerospace Engineering Department, University of California, Los Angeles, Los Angeles, 90095, CA, USA
[d] Earth and Ecosystem Science Program, Central Michigan University, Mount Pleasant, 48859, MI, USA

ARTICLE INFO

Keywords:
Moving loads
Smart road/city
Weigh-in-motion
Wave source inversion
Discretize-then-optimize (DTO) approach
Experimental validation

ABSTRACT

This paper discusses a source inversion method for the reconstruction of moving or stationary wave sources on the top surface of a two-dimensional (2D) linear elastic solid. This adjoint-gradient-based source inversion method uses vibrational measurements from sensors at the top surface of the solid, which can be heterogeneous and damped, to reconstruct temporal and spatial distributions of the wave sources. The finite element method (FEM) is used to obtain wave solutions with the high-resolution discretization of source functions in space and time leading the number of inversion parameters to range in the millions.

Numerical experiments, in which the iterative inversion procedure begins with an initial guess of zero loading at all points in space and time, show that the presented approach is effective at reconstructing horizontal and vertical components of force (i.e., normal and shear tractions) for multiple simultaneous moving dynamic distributed loads without any prior knowledge about the loads except that all loading is applied along the top surface of the solid. Provided that moving loads on roadways are applied to the top surface, it is shown that updating the guessed loading at just surface nodes, rather than at all nodes in space, greatly improves the inversion results. The inversion is shown to be as effective at reconstructing loads on the top surface of a solid when the solid is horizontally layered with multiple materials as when the solid it is homogeneous. Reducing the distance between sensors improves the accuracy of the inversion while reducing the width of distributed loads leads to less accurate results. The authors also validate the presented inversion method by using experimental data obtained from lab-scale tests at a high frequency (100 kHz) for a stationary load on a homogeneous solid.

1. Introduction

The authors of this paper are interested in a numerical algorithm that can identify the full profile of an arbitrary number of moving or stationary vibrational sources on solids of a multi-dimensional setting by using sparsely-measured wave motion data from the solids. Such an algorithm for identifying spatial and temporal profiles of loads acting on the surface of a solid can contribute to reconstructing and monitoring of the dynamic response of the pavement layer of a roadway and its sublayers, railways, or structural components, such as bridge decks or girders subject to moving loads. Namely, the algorithm can provide engineers with the ground-truth profiles of traction exerted by moving objects on transportation infrastructure (e.g., trucks, trains, airplanes on runways). The profiles of traction could include its time-dependent spatial distribution: moving speed, moving direction, frequency contents, and amplitudes. As such, the new algorithm can be used for replaying the vibrational responses of the considered transportation structures and indicate where and when stress waves of large-valued amplitudes take place within the structures due to such traction. Thus, it can help the users know the time history of large-amplitude stress waves for the considered structures. The algorithm allows structural engineers to establish a performance-based engineering tool to monitor the effect of vehicle loadings of large amplitudes on critical transportation infrastructure. On the other hand, identification of the profile of stationary wave sources can be also useful as follows. First, engineers can detect locations of impacts in complex structures, such as aerospace composite structures and, thus, localize impact-induced damages (e.g., delamination in aircraft wings) [1–6]. The source identification can also be used for other acoustic emission (AE) applications that, thus far, mostly rely on signal-processing techniques such as wavelet transform [7,8]. At the same time, source localization and characterization are crucial for the success

* Corresponding author at: School of Engineering and Technology, Central Michigan University, Mount Pleasant, 48859, MI, USA.
E-mail address: jeong1c@cmich.edu (C. Jeong).

https://doi.org/10.1016/j.ultras.2022.106880
Received 28 January 2022; Received in revised form 20 July 2022; Accepted 17 October 2022
Available online 1 November 2022

of guided wave-based mobile robotic inspection systems [9,10]. That is, structural features, such as edges and stiffeners [11], need to be identified and differentiated from damages, such as cracks and delaminations [12]. Identification of the profile of stationary wave sources can also detect falls of elderly people in buildings, improving home care of seniors [13–22].

There have been studies on (*i*) modeling the dynamic behaviors of solids/structures subject to moving sources and (*ii*) detecting moving vibrational sources on them by using sparsely-measured vibrational data as follows. There have been studies on computing dynamic behaviors, induced by moving vibration sources, of Euler–Bernoulli beams—e.g., simply supported beams or multi-span continuous beams [23–27]. Raftoyiannis et al. [28] studied the dynamic response of floating bridges of a beam model subject to buoyancy forces and/or moving loads on the bridge deck by solving the nonlinear dynamic equation. Toscano Correa et al. [29] investigated the dynamic behaviors of frictionally damped Euler–Bernoulli beams on a Winkler-type foundation under vehicle forces. The dynamic responses of an inclined beam with a moving load are studied in consideration of the effect of the axial component of the vertical load on the stiffness capacity of the beam and the associated structural stability problem [30]. An approximated formula in the closed-form was studied for evaluating the maximum response of the resonant behaviors of beam-model bridges on viscoelastic supports subject to moving loads [31]. In addition to such studies on the dynamic behaviors of a 1D beam-model structure due to moving loads, research has been conducted on the dynamic behavior of 2D or 3D solids induced by moving loads. Celebi and Schmid [32] studied the three-dimensional dynamic response of the free field near railway lines induced by moving train loads by using the thin layer method and the boundary element method. Wu [33] investigated the dynamic responses of an inclined plate subject to moving loads, presenting the effect of the inclined angle of the plate, moving-load speed, and the number of the moving loads on the plate's dynamic responses. To model ground-borne vibration with a significant reduction of the number of degrees-of-freedom in a curved track–tunnel–soil system excited by moving railway traffic loads, a curved two-and-a-half-dimensional (2.5D) model was investigated [34]. Ma et al. [35] extended the curved 2.5D model by coupling the curved 2.5D finite elements and perfectly-matched-layers (PML) elements to study the wave propagations in longitudinally curved tunnel-ground systems, of which laterally-propagating waves being emitted to the far field, are modeled by the PML [36,37].

As methods for detecting moving vibrational sources on beam structures/solids by using sparsely-measured vibrational data, the Genetic Algorithm (GA)-based minimization method has been employed to detect the properties of moving loads on beam structures. Au et al. [23] investigated a multiple-level GA—adjusting the range of the parameter values during the inversion process—so that the optimizer avoids the local minimum of a minimization function. Jeong et al. [38] investigated the GA-based minimization method to identify several moving wave sources of an arbitrary number in a 1D solid setting. However, GA-based acoustic source inversion (ASI) methods are effective only when the number of unknown load parameters is small, as shown in [38]. In addition, there have been studies on a passive moving wave source-based structural health monitoring (SHM) approach, by which engineers can take advantage of ambient vibration sources, such as vehicles on roadways or trains on railroads in order to monitor the structural integrity. Mei et al. [39] presented a theoretical and experimental study for the detection of structural damages by using sensors on passing-by vehicles and considering vehicle–bridge dynamic interaction. The GA method was also useful for simultaneously identifying the speed, acceleration, frequency, and amplitude of a moving load on a Timoshenko-beam bridge model and the anomaly (e.g., reduction due to damage) in the elastic modulus of the bridge by using the measurement data of bridge vibration [40]. Recently, Lloyd and Jeong have investigated an adjoint equation-based inverse-moving source method for identifying the spatial and temporal distribution of wave sources, which are either moving or stationary, in a 1D heterogeneous undamped solid [41]. Lloyd and Jeong also introduced the discretize-then-optimize (DTO) approach to solving the inverse-moving source problem considering a 1D heterogeneous damped solid truncated by a wave-absorbing boundary condition (WABC) [42]. However, these studies [41,42] have been conducted primarily in 1D settings. The literature is still sparse on the adjoint equation-based inversion methods to detect the spatial and temporal distributions of moving sources in 2D solids or 3D solid settings. Such a potential method can be also employed, without the loss of generality, for detecting the profile of a stationary wave source.

To fill this gap, the presented paper contributes to the body of knowledge by presenting a new adjoint equation-based numerical method for identifying arbitrary wave sources on a 2D, bounded, heterogeneous, damped solid. The control parameters are all the discretized parameters of the possible distributions of the wave sources in all the discrete locations within/on the domain and all the time steps during the observation time so that the total number of the parameters could be as large as several million or more. To update such a large number of inversion parameters, a gradient-based minimization method is used in which the gradient of a misfit function is determined in an analytical fashion by the PDE-constrained optimization approach. The accuracy and computational efficiency of computing the gradient during the full-waveform inversion (FWI) process are superior and do not depend on the number of the parameters. The authors' mathematical modeling accurately takes into account the wave physics—such as reflection, refraction, and damping—in the solid. The discretized-then-optimize (DTO) approach enables such mathematical modeling in a systematical and compact manner while considering all the physics of interest. As the strength of the presented algorithm, it does not need to have any prior knowledge about targeted sources (e.g., their numbers, excitational frequency contents, initial locations, moving directions, moving speeds, and accelerations). Even without such a-prior knowledge, the algorithm is capable of reconstructing the spatial and temporal distributions of sources of an arbitrary number on a 2D bounded heterogeneous, damped solid. The authors also experimentally validate the presented algorithm by testing the feasibility to determine the profile of a wave source in a 2D plane-stress setting by using the presented algorithm with real experimental measurement data in a laboratory.

The presented paper is comprised of the following. (*i*) The problem definition introduces the goal of this research and the governing wave equation and its associated conditions; (*ii*) The forward wave modeling section describes the finite element modeling of wave responses of a 2D solid subject to vibrational tractions; (*iii*) The inverse modeling section presents the DTO approach to identifying a wave source profile using sparsely-measured wave motion data; (*iv*) The numerical experiments section shows a number of examples on parametric studies; and (*v*) Lastly, the experimental validation of this method is presented.

2. Problem definition

As the goal of this research, the authors study a new numerical method to identify the spatial and temporal distribution of moving or stationary wave sources on the top surface of the 2D damped, heterogeneous solid by using measured vibrational motion data. As experimental validation of the presented new numerical method, the authors identify the spatial and temporal distribution of traction induced by a transducer on the top surface of a solid specimen by using this new numerical method with real measurement data (of a frequency with the order of magnitude about 100 kHz) from a lab experiment. Although the experiment was performed by using a stationary wave source in a small lab scale, the validation could potentially show the feasibility of using the presented method with vibration measurement data on a large-scale realistic transportation structure subject to moving sources of a frequency with a lower order of magnitude, e.g., 10 to 100 Hz.

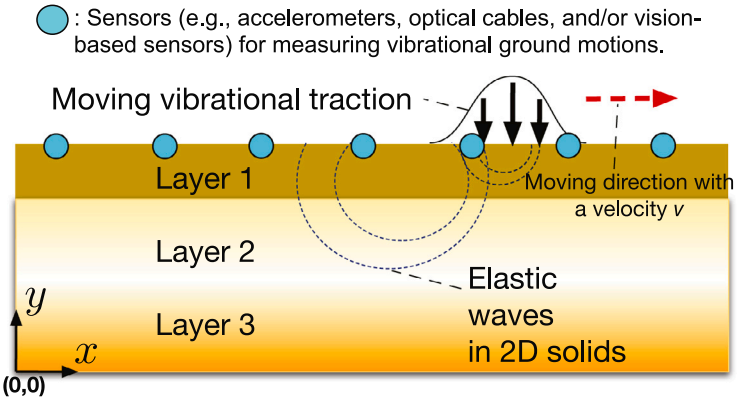

Fig. 1. Exemplary two-dimensional (2D) model of a multi-layered solid with a moving or stationary dynamic distributed load on the top surface. The solid is fixed along the bottom boundary, and vibrational motions are sparsely measured at the top surface.

2.1. Governing wave physics

The 2D model considered in this study is a rectangular solid with height, H, and length, L, that is fixed along the bottom edge, $y = 0$. This model configuration is shown in Fig. 1. The top and side surfaces of the rectangular solid are traction-free. The solid is initially at rest everywhere. One or more targeted moving or stationary dynamic distributed loads are applied to the top surface, $y = H$, while sensors at or near the surface provide measured vibrational motion data. For this study, the sensors considered measure both x- and y-components of displacement field of wave responses or only y-components of them. The users of the presented method can use accelerometers, distributed acoustic sensors (DAS), or vision-based motion sensors as sensors.

In the presented numerical method, a 2D plane-strain setting can be considered: the thickness of the solid in the z-direction is much larger than its x- and y-dimensions, and the cross-section and external forces do not vary in the z-direction. A 2D plane-stress setting can also be considered, by simply changing the elasticity tensor, for the numerical method presented, which is particularly useful for the lab-scale experimental validation.

The solid can be homogeneous or consist of layers of different materials as shown in Fig. 1. The governing wave equation for the domain, Ω, is:

$$\nabla \cdot \boldsymbol{\sigma} - \alpha \dot{\mathbf{u}} + \mathbf{b} = \rho \ddot{\mathbf{u}} \quad \text{in } \Omega, \tag{1}$$

where $\boldsymbol{\sigma}$ denotes the stress tensor, $\mathbf{b}$ is the body force vector, α represents a damping coefficient, ρ is the density, and $\mathbf{u} = [u_x, u_y]$ represents the displacements. The material constitutive equation is:

$$\boldsymbol{\sigma} = \mathbf{c}\varepsilon, \tag{2}$$

where $\mathbf{c}$ is the elasticity tensor and ε is the strain tensor. For the plane-strain setting, $\mathbf{c}$ is:

$$\mathbf{c} = \frac{E(1-\nu)}{(1+\nu)(1-2\nu)} \begin{bmatrix} 1 & \frac{\nu}{1-\nu} & 0 \\ \frac{\nu}{1-\nu} & 1 & 0 \\ 0 & 0 & \frac{1-2\nu}{2(1-\nu)} \end{bmatrix}, \tag{3}$$

where E is the modulus of elasticity, ν is Poisson's ratio. For the plane-stress setting, $\mathbf{c}$ is

$$\mathbf{c} = \frac{E}{1-\nu^2} \begin{bmatrix} 1 & \nu & 0 \\ \nu & 1 & 0 \\ 0 & 0 & \frac{1-\nu}{2} \end{bmatrix}. \tag{4}$$

The initial conditions are:

$$u(x, y, t) = 0, \quad 0 \le x \le L, \quad 0 \le y \le H, \quad t = 0, \tag{5}$$

$$\frac{\partial u(x, y, t)}{\partial t} = 0, \quad 0 \le x \le L, \quad 0 \le y \le H, \quad t = 0. \tag{6}$$

The boundary conditions at the bottom boundary is:

$$u(x, 0, t) = 0, \quad 0 \le x \le L, \quad 0 \le t \le T. \tag{7}$$

The right hand and left hand boundaries of the solid are traction free for all times, t:

$$\boldsymbol{\sigma}\mathbf{n} = \mathbf{0}. \tag{8}$$

On the top surface, the moving loads applied may have x and y components of traction and are dynamic, distributed loads:

$$\boldsymbol{\sigma}\mathbf{n} = \begin{bmatrix} f_x(x, t) \\ f_y(x, t) \end{bmatrix}, \tag{9}$$

where $f_x(x, t)$ and $f_y(x, t)$ are traction functions of x and t given $0 \le x \le L$ and $0 \le t \le T$.

It should be noted that the aforementioned boundary conditions represent those of a specific case. However, the presented inversion modeling approach can straightforwardly accommodate various boundary conditions by virtue of the DTO modeling. For instance, the left, right, and bottom boundaries can be modeled as wave-absorbing boundary conditions, such as perfectly-matched-layers (PMLs) [36] to model the infinite extent of a roadway model.

3. Forward wave modeling

The solution of the governing wave equation is numerically computed by using the Galerkin finite element method (FEM). To this end, the finite-element approximation of the solution is introduced as the following:

$$\mathbf{u}(x, y, t) = \begin{bmatrix} u_x(x, y, t) = \boldsymbol{\Phi}(x, y)^T \mathbf{u}_x(t) \\ u_y(x, y, t) = \boldsymbol{\Phi}(x, y)^T \mathbf{u}_y(t) \end{bmatrix},$$
$$\mathbf{w}(x, y) = \begin{bmatrix} w_x(x, y) = \mathbf{w}_x^T \boldsymbol{\Phi}(x, y) \\ w_y(x, y) = \mathbf{w}_y^T \boldsymbol{\Phi}(x, y) \end{bmatrix}, \tag{10}$$

where $\boldsymbol{\Phi}$ denotes a vector of a global basis functions constructed by the shape functions of a 9-node quadratic, quadrilateral element, and $\mathbf{u}_x(t)$ and $\mathbf{u}_y(t)$ are the solution vectors in all nodes at time t while $\mathbf{w}_x$ and $\mathbf{w}_x$ are their test-function counterparts. Then, the wave equation (1) for the solid can be expressed in a matrix form as:

$$\mathbf{K}\mathbf{s}(t) + \mathbf{C}\dot{\mathbf{s}}(t) + \mathbf{M}\ddot{\mathbf{s}}(t) = \mathbf{f}(t), \tag{11}$$

where

$$\mathbf{s}(t) = \begin{bmatrix} \mathbf{u}_x(t) \\ \mathbf{u}_y(t) \end{bmatrix}, \tag{12}$$

and $\mathbf{K}$, $\mathbf{C}$, and $\mathbf{M}$ are the stiffness, damping, and mass matrices. The mass matrix is defined as:

$$\mathbf{M} = \begin{bmatrix} \mathbf{M}_{xx} & \mathbf{0} \\ \mathbf{0} & \mathbf{M}_{yy} \end{bmatrix}, \tag{13}$$

where the submatrices, $\mathbf{M}_{xx}$ and $\mathbf{M}_{yy}$, are:

$$\mathbf{M}_{xx} = \int_{\Omega} \rho \boldsymbol{\Phi}\boldsymbol{\Phi}^T d\Omega,$$
$$\mathbf{M}_{yy} = \int_{\Omega} \rho \boldsymbol{\Phi}\boldsymbol{\Phi}^T d\Omega. \tag{14}$$

The damping matrix is defined as:

$$\mathbf{C} = \begin{bmatrix} \mathbf{C}_{xx} & \mathbf{0} \\ \mathbf{0} & \mathbf{C}_{yy} \end{bmatrix}, \tag{15}$$

where the submatrices, $\mathbf{C}_{xx}$ and $\mathbf{C}_{yy}$, are:

$$\mathbf{C}_{xx} = \int_{\Omega} \alpha \boldsymbol{\Phi}\boldsymbol{\Phi}^T d\Omega,$$
$$\mathbf{C}_{yy} = \int_{\Omega} \alpha \boldsymbol{\Phi}\boldsymbol{\Phi}^T d\Omega. \tag{16}$$

The stiffness matrix is defined as:

$$\mathbf{K} = \begin{bmatrix} \mathbf{K}_{xx} & \mathbf{K}_{xy} \\ \mathbf{K}_{yx} & \mathbf{K}_{yy} \end{bmatrix}, \tag{17}$$

where the submatrices, $\mathbf{K}_{xx}$, $\mathbf{K}_{xy}$, $\mathbf{K}_{yx}$, and $\mathbf{K}_{yy}$, are:

$$\mathbf{K}_{xx} = \int_{\Omega} \left(\frac{E(1-\nu)}{(1+\nu)(1-2\nu)} \right) \frac{\partial \boldsymbol{\Phi}}{\partial x} \frac{\partial \boldsymbol{\Phi}}{\partial x}^T + \left(\frac{E}{2(1+\nu)} \right) \frac{\partial \boldsymbol{\Phi}}{\partial y} \frac{\partial \boldsymbol{\Phi}}{\partial y}^T d\Omega,$$
$$\mathbf{K}_{xy} = \int_{\Omega} \left(\frac{E}{2(1+\nu)} \right) \frac{\partial \boldsymbol{\Phi}}{\partial y} \frac{\partial \boldsymbol{\Phi}}{\partial x}^T + \left(\frac{E\nu}{(1+\nu)(1-2\nu)} \right) \frac{\partial \boldsymbol{\Phi}}{\partial x} \frac{\partial \boldsymbol{\Phi}}{\partial y}^T d\Omega,$$
$$\mathbf{K}_{yx} = \int_{\Omega} \left(\frac{E}{2(1+\nu)} \right) \frac{\partial \boldsymbol{\Phi}}{\partial x} \frac{\partial \boldsymbol{\Phi}}{\partial y}^T + \left(\frac{E\nu}{(1+\nu)(1-2\nu)} \right) \frac{\partial \boldsymbol{\Phi}}{\partial y} \frac{\partial \boldsymbol{\Phi}}{\partial x}^T d\Omega,$$
$$\mathbf{K}_{yy} = \int_{\Omega} \left(\frac{E(1-\nu)}{(1+\nu)(1-2\nu)} \right) \frac{\partial \boldsymbol{\Phi}}{\partial y} \frac{\partial \boldsymbol{\Phi}}{\partial y}^T + \left(\frac{E}{2(1+\nu)} \right) \frac{\partial \boldsymbol{\Phi}}{\partial x} \frac{\partial \boldsymbol{\Phi}}{\partial x}^T d\Omega. \tag{18}$$

The matrices $\mathbf{K}$, $\mathbf{C}$, and $\mathbf{M}$ are symmetric. The force vector $\mathbf{f}(t)$ is defined as:

$$\mathbf{f}(t) = \begin{bmatrix} \mathbf{f}_x(t) \\ \mathbf{f}_y(t) \end{bmatrix}, \tag{19}$$

where

$$\mathbf{f}_x(t) = \int_{\Gamma_{\text{loaded}}} f_x(x,t) \boldsymbol{\Phi}\, d\Gamma,$$
$$\mathbf{f}_y(t) = \int_{\Gamma_{\text{loaded}}} f_y(x,t) \boldsymbol{\Phi}\, d\Gamma. \tag{20}$$

Eq. (11) per each ith time step is written as:

$$\mathbf{K}\mathbf{s}_i + \mathbf{C}\dot{\mathbf{s}}_i + \mathbf{M}\ddot{\mathbf{s}}_i = \mathbf{f}_i \tag{21}$$

where $\mathbf{s}_i$ is the solution vector of $\mathbf{s}(t)$ at the ith time step, the system of equations is solved using Newmark time integration. The Newmark time integration steps can be written in the following compact form:

$$\mathbf{Q}\hat{\mathbf{s}} = \hat{\mathbf{f}}, \tag{22}$$

where the vectors $\hat{\mathbf{s}}$ and $\hat{\mathbf{f}}$, for all the time steps, are built as:

$$\hat{\mathbf{s}} = \begin{bmatrix} \mathbf{s}_0 \\ \dot{\mathbf{s}}_0 \\ \ddot{\mathbf{s}}_0 \\ \mathbf{s}_1 \\ \dot{\mathbf{s}}_1 \\ \ddot{\mathbf{s}}_1 \\ \vdots \\ \mathbf{s}_{N_i} \\ \dot{\mathbf{s}}_{N_i} \\ \ddot{\mathbf{s}}_{N_i} \end{bmatrix}, \quad \hat{\mathbf{f}} = \begin{bmatrix} \mathbf{0} \\ \mathbf{0} \\ \mathbf{f}_0 \\ \mathbf{f}_1 \\ \mathbf{0} \\ \mathbf{0} \\ \vdots \\ \mathbf{f}_{N_i} \\ \mathbf{0} \\ \mathbf{0} \end{bmatrix}. \tag{23}$$

The vector $\mathbf{s}_{N_i}$ contains the displacements at every node for the final time step, N_i, and the vector $\mathbf{f}_{N_i}$ contains the forces at every node for the final time step, N_i. There are x- and y-components of displacement and force so $\mathbf{s}_{N_i}$ and $\mathbf{f}_{N_i}$ each have the order $2N_j \times 1$ where N_j is the number of nodes. Therefore, the vectors $\hat{\mathbf{s}}$ and $\hat{\mathbf{f}}$ each have the order $3(2N_j)(N_i+1)\times 1$. The Q matrix in Eq. (22) is defined as [42]:

$$\mathbf{Q} = \begin{bmatrix} \mathbf{I} & \mathbf{0} & \mathbf{0} & \mathbf{0} & \mathbf{0} & \mathbf{0} & \dots & \mathbf{0} & \mathbf{0} & \mathbf{0} & \mathbf{0} & \mathbf{0} & \mathbf{0} \\ \mathbf{0} & \mathbf{I} & \mathbf{0} & \mathbf{0} & \mathbf{0} & \mathbf{0} & \dots & \mathbf{0} & \mathbf{0} & \mathbf{0} & \mathbf{0} & \mathbf{0} & \mathbf{0} \\ \mathbf{K} & \mathbf{C} & \mathbf{M} & \mathbf{0} & \mathbf{0} & \mathbf{0} & \dots & \mathbf{0} & \mathbf{0} & \mathbf{0} & \mathbf{0} & \mathbf{0} & \mathbf{0} \\ \mathbf{L}_1 & \mathbf{L}_2 & \mathbf{L}_3 & \mathbf{K}_{\text{eff}} & \mathbf{0} & \mathbf{0} & \dots & \mathbf{0} & \mathbf{0} & \mathbf{0} & \mathbf{0} & \mathbf{0} & \mathbf{0} \\ a_1\mathbf{I} & \mathbf{I} & \mathbf{0} & -a_1\mathbf{I} & \mathbf{I} & \mathbf{0} & \dots & \mathbf{0} & \mathbf{0} & \mathbf{0} & \mathbf{0} & \mathbf{0} & \mathbf{0} \\ a_0\mathbf{I} & a_2\mathbf{I} & \mathbf{I} & -a_0\mathbf{I} & \mathbf{0} & \mathbf{I} & \dots & \mathbf{0} & \mathbf{0} & \mathbf{0} & \mathbf{0} & \mathbf{0} & \mathbf{0} \\ \vdots & \vdots & \vdots & \vdots & \vdots & \vdots & \ddots & \vdots & \vdots & \vdots & \vdots & \vdots & \vdots \\ \mathbf{0} & \mathbf{0} & \mathbf{0} & \mathbf{0} & \mathbf{0} & \mathbf{0} & \dots & \mathbf{L}_1 & \mathbf{L}_2 & \mathbf{L}_3 & \mathbf{K}_{\text{eff}} & \mathbf{0} & \mathbf{0} \\ \mathbf{0} & \mathbf{0} & \mathbf{0} & \mathbf{0} & \mathbf{0} & \mathbf{0} & \dots & a_1\mathbf{I} & \mathbf{I} & \mathbf{0} & -a_1\mathbf{I} & \mathbf{I} & \mathbf{0} \\ \mathbf{0} & \mathbf{0} & \mathbf{0} & \mathbf{0} & \mathbf{0} & \mathbf{0} & \dots & a_0\mathbf{I} & a_2\mathbf{I} & \mathbf{I} & -a_0\mathbf{I} & \mathbf{0} & \mathbf{I} \end{bmatrix}, \tag{24}$$

where

$$\mathbf{K}_{\text{eff}} = a_0\mathbf{M} + a_1\mathbf{C} + \mathbf{K},$$
$$\mathbf{L}_1 = -a_0\mathbf{M} - a_1\mathbf{C},$$
$$\mathbf{L}_2 = -a_2\mathbf{M} - \mathbf{C},$$
$$\mathbf{L}_3 = -\mathbf{M}, \tag{25}$$

and

$$a_0 = \frac{4}{(\Delta t)^2}, \quad a_1 = \frac{2}{\Delta t}, \quad a_2 = \frac{4}{\Delta t}. \tag{26}$$

The $\mathbf{Q}$ matrix has the order $3(2N_j)(N_i+1)\times 3(2N_j)(N_i+1)$ where N_j is the number of nodes, and N_i is the number of time steps. The in-house forward wave solver, based on the Newmark time integration scheme, used in this study is verified by comparing its solution with that from an academic FEM software, FEAP [43]. Details of this verification against FEAP are omitted in this paper for brevity.

4. Inverse modeling

To reconstruct targeted moving or stationary wave sources by using measured vibrational data, guessed loads are iteratively updated to minimize the misfit between measured wave responses, induced by unknown targeted wave sources, and computed wave responses generated by the guessed sources.

4.1. Discrete objective and Lagrangian functionals

Under this work, the following objective functional in a continuous form is minimized:

$$\mathcal{L} = \int_0^T \sum_{q=1}^{N_q} (\mathbf{u}_{\text{m}_q} - \mathbf{u}_q) \cdot (\mathbf{u}_{\text{m}_q} - \mathbf{u}_q) dt, \tag{27}$$

where $\mathbf{u}_{\text{m}_q}$ is the measured displacement at the qth sensor, $\mathbf{u}_q$ is the computed displacement at qth sensor based on the guessed loading, and N_q is the number of sensors. The interval $t = 0$ to T is the time period, for which wave responses are observed. The discrete-form counterpart of Eq. (27) is:

$$\hat{\mathcal{L}} = (\hat{\mathbf{s}}_{\text{m}} - \hat{\mathbf{s}})^T \bar{\mathbf{B}} (\hat{\mathbf{s}}_{\text{m}} - \hat{\mathbf{s}}), \tag{28}$$

where $\bar{\mathbf{B}}$ is a block diagonal matrix defined as $\bar{\mathbf{B}} = \Delta t\mathbf{B}$, and $\mathbf{B}$ has values of one at diagonal elements corresponding to displacements at nodes, where sensors are located, and zero everywhere else.

By imposing the compact discrete form, Eq. (22), of the wave problem onto the discrete objective functional, through the use of Lagrange multiplier, $\hat{\lambda}$, the following Lagrangian functional is built:

$$\hat{\mathcal{A}} = (\hat{\mathbf{s}}_{\text{m}} - \hat{\mathbf{s}})^T \bar{\mathbf{B}} (\hat{\mathbf{s}}_{\text{m}} - \hat{\mathbf{s}}) - \hat{\lambda}^T \left(\mathbf{Q}\hat{\mathbf{s}} - \hat{\mathbf{f}} \right). \tag{29}$$

4.2. The first order optimality conditions

In order to determine the estimated control parameters that lead to the vanishing gradient of the objective functional, the following optimality conditions must be satisfied:

$$\frac{\partial \hat{\mathcal{A}}}{\partial \hat{\lambda}} = 0: \quad \text{The first condition (state problem),} \tag{30}$$

$$\frac{\partial \hat{\mathcal{A}}}{\partial \hat{\mathbf{s}}} = 0: \quad \text{The second condition (adjoint problem),} \tag{31}$$

$$\frac{\partial \hat{\mathcal{A}}}{\partial \hat{\mathbf{f}}} = 0: \quad \text{The third condition (control problem).} \tag{32}$$

Each condition above is described as follows.

4.2.1. The first optimality condition

First, taking the derivative of Eq. (29) with respect to the Lagrange multiplier, $\hat{\lambda}$, gives the following:

$$\frac{\partial \hat{\mathcal{A}}}{\partial \hat{\lambda}} = -\mathbf{Q}\hat{\mathbf{s}} + \hat{\mathbf{f}} = 0. \tag{33}$$

This first optimality condition is automatically satisfied by obtaining the solution of the discrete forward problem Eq. (22).

4.2.2. The second optimality condition

Setting the derivative of the discrete Lagrangian with respect to $\hat{\mathbf{s}}$ to vanish gives the following:

$$\frac{\partial \hat{\mathcal{A}}}{\partial \hat{\mathbf{s}}} = 2\bar{\mathbf{B}}(\hat{\mathbf{s}} - \hat{\mathbf{s}}_{\mathrm{m}}) - \mathbf{Q}^T \hat{\lambda} = 0. \tag{34}$$

Because Eq. (34) involves the transpose of Q and the final conditions are known, the reverse Newmark time integration is then used to solve for the Lagrange multiplier solution vector, λ, at every time step backtracking from the final time step to the initial time step.

4.2.3. The third optimality condition

For having the derivative of the Lagrangian functional $\hat{\mathcal{A}}$ with respect to the vector of control parameters $\hat{\mathbf{f}}$ equal to zero, the desired control parameters satisfy the following discrete control equation:

$$\frac{\partial \hat{\mathcal{A}}}{\partial \hat{\mathbf{f}}} = \hat{\lambda} = 0. \tag{35}$$

The side-imposed part of the Lagrangian functional always vanishes once the state problem is solved. Therefore, the gradient of the discrete objective and Lagrangian functional with respect to $\hat{\mathbf{f}}$ can thus be written as:

$$\frac{\partial \hat{\mathcal{A}}}{\partial \hat{\mathbf{f}}} = \frac{\partial \hat{\mathcal{L}}}{\partial \hat{\mathbf{f}}} = \hat{\lambda}. \tag{36}$$

Only the components of $\hat{\lambda}$ that correspond to the degrees of freedom and time steps of the non-zero force components of $\hat{\mathbf{f}}$ in Eq. (23) comprise the gradient vector, $\hat{\mathbf{g}}$, such that:

$$\hat{\lambda} = \begin{bmatrix} \lambda_0 \\ \dot{\lambda}_0 \\ \ddot{\lambda}_0 \\ \lambda_1 \\ \dot{\lambda}_1 \\ \ddot{\lambda}_1 \\ \vdots \\ \lambda_{N_i} \\ \dot{\lambda}_{N_i} \\ \ddot{\lambda}_{N_i} \end{bmatrix}, \quad \hat{\mathbf{g}} = \begin{bmatrix} \mathbf{0} \\ \mathbf{0} \\ \mathbf{g}_0 \\ \mathbf{g}_1 \\ \mathbf{0} \\ \mathbf{0} \\ \vdots \\ \mathbf{g}_{N_i} \\ \mathbf{0} \\ \mathbf{0} \end{bmatrix} = \begin{bmatrix} \mathbf{0} \\ \mathbf{0} \\ \ddot{\lambda}_0 \\ \lambda_1 \\ \mathbf{0} \\ \mathbf{0} \\ \vdots \\ \lambda_{N_i} \\ \mathbf{0} \\ \mathbf{0} \end{bmatrix}. \tag{37}$$

The vectors $\hat{\lambda}$ and $\hat{\mathbf{g}}$ contain the Lagrange multipliers and gradients, respectively, for x- and y-components at all nodal points in space and time. Each $\hat{\lambda}$ and $\hat{\mathbf{g}}$ have the order $3(2N_j)(N_i+1)\times 1$ where N_j is the number of nodes and N_i is the number of time steps.

4.3. The parameter-updating scheme

By using the conjugate gradient method, the estimated loading is updated in the following way:

$$\hat{\mathbf{f}}_{n+1} = \hat{\mathbf{f}}_n + h_n \hat{\mathbf{d}}_n, \tag{38}$$

where $\hat{\mathbf{f}}_n$ is the guessed loading at the nth iteration, h_n is a step size, and $\hat{\mathbf{d}}_n$ is the search direction based on the following conjugate-gradient calculation: for $n = 0$ and every mth iteration, $\hat{\mathbf{d}}_n = -\hat{\mathbf{g}}_n$, and for $n \geq 1$ except every mth iteration, $\hat{\mathbf{d}}_n = -\hat{\mathbf{g}}_n + \frac{\hat{\mathbf{g}}_n \cdot \hat{\mathbf{g}}_n}{\hat{\mathbf{g}}_{n-1} \cdot \hat{\mathbf{g}}_{n-1}} \hat{\mathbf{d}}_{n-1}$. Namely, the search direction is reset at every mth iteration to $-\hat{\mathbf{g}}_n$ to avoid errors potentially accumulated over the iterations of calculating the search direction. In this study, $m = 50$ is used, and it is chosen from a trial and error considering a few choices of m from 1 to 50.

Given that it is reasonable to assume that the unknown vibrational load is located on the top surface of the 2D solid, Eq. (38) can be modified to only update the guessed loading at surface nodes (instead of entire nodes in the solid domain) in the following way:

$$\hat{\mathbf{f}}_{n+1} = \hat{\mathbf{f}}_n + h_n \mathbf{D} \hat{\mathbf{d}}_n, \tag{39}$$

where $\mathbf{D}$ is a diagonal matrix that has values of one at diagonal elements that correspond to nodes located on the top surface and zero everywhere else. In this study, the optimal step size h_n—i.e., the step size for which the resulting updated estimated loading causes the objective functional to decrease the most—is determined by using Newton's method, the details of which can be found in [41].

5. Numerical experiments of moving-source inversion

To demonstrate the performance of the presented inversion algorithm to reconstruct the targeted loads, numerical experiments are conducted with one or more moving loads applied to the top surface of a 2D solid serving as targets. A 2D FEM model, with a length of $L = 60$ m and a height of $H = 20$ m, is used for each example in the presented numerical experiments. The FEM model uses nine-node 1 m × 1 m square, quadratic elements and the observation period is $T = 2$ s with a time step size of $\Delta t = 0.002$ s.

With 4961 nodes in the entire domain, two force component directions (x and y), and 1001 time steps, including the initial step, there could be at most $4961 \times 2 \times 1001 = 9,931,922$ control parameters that can discretize estimated wave source functions. However, if an estimated loading is updated at the top surface only, as in Eq. (39), $121 \times 2 \times 1001 = 242,242$ guessed parameters are updated each iteration. The initial guess for each example case is $\hat{\mathbf{f}}_0 = 0$, i.e., the x and y components of estimated force at all points in space (i.e., the entire domain or the top surface) and time in the model are set to be zero. In the following example cases, the information about target loadings—such as the number of moving loads, velocity, x-position, magnitude, or frequency of each load—is considered unknown and to be identified.

The moving dynamic distributed loads, for $0 \leq t \leq T$, are defined by the following:

$$f_x(x,H,t) = \sum_{k=1}^{N_k} P_x(t)_k \mathrm{e}^{-\frac{(x-b(t)_k)^2}{2d_k^2}}, \quad 0 \leq x \leq L \tag{40}$$

$$f_y(x,H,t) = \sum_{k=1}^{N_k} P_y(t)_k \mathrm{e}^{-\frac{(x-b(t)_k)^2}{2d_k^2}}, \quad 0 \leq x \leq L \tag{41}$$

where N_k is number of the moving distributed loads; $P_x(t)_k$ and $P_y(t)_k$ are the time-varying amplitudes at the peak point of the kth load in the x- and y-directions respectively; $b(t)_k$ defines the position of the central peak of the load; and d_k controls the horizontal width of the distribution of the load. The full width at a tenth of the maximum (FWTM)—see the visualization of FWTM in Fig. 2—of the amplitude of the kth target moving load is used to approximate the width of the distribution of

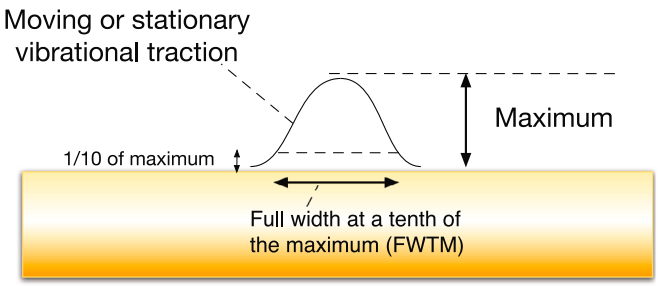

Fig. 2. The full width at a tenth of the maximum (FWTM) of a distributed moving or stationary traction.

each target load and has the following relationship to d_k:

$$d_k = \frac{\text{FWTM of the } k\text{th target force amplitude}}{2\sqrt{2\ln 10}}. \tag{42}$$

To assess the inversion results in the following numerical experiments, the error between the estimated loading and the target loading is calculated using the following normalized mean absolute error:

$$\epsilon = \frac{\frac{1}{N_p}\sum_{i=1}^{N_i}\sum_{j=1}^{N_j}|f_{ij_{\text{target}}} - f_{ij_{\text{estimate}}}|}{\frac{1}{N_p}\sum_{i=1}^{N_i}\sum_{j=1}^{N_j}|f_{ij_{\text{target}}}|} \tag{43}$$

where N_i is the number of points in time, N_j is the number of points in space, and N_p is the total number of points in space and time. This error considers the loads at all nodal points in space and time in the problem, i.e. all the control parameters in the problem. It is normalized while avoiding dividing by zero, which would happen if another type of error (e.g., the mean percentage error) is used. The authors agree that the errors, computed using (43), may have large values, especially even when the inversion method appears to get good results. However, the normalized mean absolute error is still helpful in judging whether the inversion results improve with increasing iterations and how the inversion results compare across different examples and cases that have the same target loads. Alternatively, this work could (a) extract velocity, acceleration, initial position, amplitude, and frequencies from the final inverted force distribution and (b) compare them with targeted counterparts. It may, though, need another algorithm to extract those but reduce the value of the error.

5.1. Example 1: Updating an estimated loading at every node within the domain versus only at the nodes along the top surface

In Example 1, the performance of the presented moving-source inversion—(a) when the guessed loading is updated at every node in the entire domain of interest each iteration—is compared to that—(b) when the guessed loading is updated only at the nodes along the top surface by examining the following two cases.

- Case 1a: The guesses for the x- and y-components of force at each node point in the entire domain for each time step (i.e., 9.93 million control parameters) are updated as in Eq. (38).
- Case 1b: The guesses for the x- and y-components of force are updated only at the nodes located on the top surface of the solid for each time step (i.e., 0.24 million control parameters) as in Eq. (39).

In Example 1, the solid consists of one material where the modulus of elasticity, density, and Poisson's ratio are $E = 25$ MPa, $\rho = 2400$ kg/m^3, and $\nu = 0.3$, respectively, representing the ground soil below the surface. For Example 1, the constant, α, has the value $\alpha = 12{,}500$ kg/(m^3 s). The sensors are located along the top surface and are spaced every three meters. A previous study by Guidio et al. [44]—on the seismic input inversion (not the moving source inversion)—suggested that, in the inverse source problem, the sensor spacing in the order of magnitude of the S-wave wavelength on the top surface leads to effective source-inversion performance. In Example 1, the smallest wavelength of Case 1 is 13 m, which corresponds to the shear wave speed of 63 m/s and the frequency of a moving wave source of 5 Hz. In example 3, the maximum frequency is 15 Hz so that the smallest wavelength is about 4.3 m. The three meter sensor spacing is smaller than the smallest S-wave wavelength so that it meets the desired sensor spacing mentioned above. In the experimental validation in Section 6, sensor spacing of 10 mm is employed whereas the smallest wavelength is 30 mm corresponding to $v_s = 3097$ m/s and the frequency of 100 kHz. For both Case 1a and Case 1b, the target loading is a vertical load applied to the top surface of the solid with $d = 1.5$ m (FWTM = 6.44 m). The time-varying amplitude, $P_y(t)$, has a static and dynamic component: $P_y(t) = -[500\sin(\omega t) + 2000]$ N/m with an angular frequency, $\omega = 2\pi(5)$ rad/s. The time-varying peak amplitudes in this study serve as examples of loading cases that can have static and dynamic components. They can be employed to model the traction from moving vibrational loads (e.g., vehicles). Namely, the static part of $P_y(t)$ represents the weight of a vehicle while its dynamic component models the vertical force caused by the rotatory vibration of a vehicle engine. If the total load under the Gaussian distribution is approximated as the area of the triangle with a base equal to FWTM and height equal to the amplitude of the static part, the largest load in the examples is $\frac{1}{2}(2000$ N/m$)(6.44$ m$) = 6440$ N, which is about half the weight of a typical compact car. However, 6.44 m and 3.22 m of FWTM are not realistic widths of surface contact for vehicles. The target load moves horizontally with an initial displacement, $x_0 = 2.5$ m, an initial velocity, $v_0 = 20$ m/s, and an acceleration, $a = 3.6$ m/s^2, so that the central peak of the target loading varies over time as $b(t) = [2.5 + 20t + 0.5(3.6)t^2]$ m based on the equation for position, $b(t) = [x_0 + v_0 t + 0.5at^2]$. Fig. 3 shows snapshots, at two different points in time, of the moving load and its corresponding displacement magnitude of wave responses $|u| = \sqrt{u_x{}^2 + u_y{}^2}$ in the domain.

The results of Example 1, with 300 iterations[1] completed, show that updating the guesses at the top surface nodes is much more effective in reconstructing the moving distributed load than updating the guesses at every node in the entire domain. Namely, Fig. 4 shows the inversion errors calculated, per Eq. (44), each iteration for Case 1a and Case 1b, presenting that the terminal value of the inversion error is smaller in Case 1b than Case 1a. Essentially, this work considerably reduces the number of unknown control parameters in the presented inverse problem by considering only the loads at nodes along the top surface as unknown. When the number of control parameters is reduced, a typical inversion solver performs more effectively than otherwise. Fig. 5 shows, in its contour plots, that the target and reconstructed loads after 300 iterations for Case 1a and Case 1b. With time as an axis, the changes in position over time of the targeted and reconstructed moving loads are displayed in Fig. 5. The contour plots show that the reconstructed loads in both Case 1a and Case 1b capture the position of the target moving load. However, the magnitude of the force on the surface in Case 1b is much closer to its targeted counterpart than in Case 1a. As the reason for such an inaccuracy of inversion in Case 1a, it can be observed, from Figs. 5(c) and 5(d) , that some body force close to the surface (e.g., see $0 \le x \le 10$, $15 \le y \le 20$, and $t = 0$) is present in the reconstructed force profile in Case 1a, while only surface loads are present for the target and the reconstruction in Case 1b. Both Case 1a

[1] 300 is defined as the authors' maximum number of iterations, which is basically chosen on trial and error, but 300 iterations is a conservative estimate for Examples 1 through 4. The error plots in Fig. 4, Fig. 7, and Fig. 11 show that the error stops improving before 100 iterations. Thus, using a high value of iterations (e.g., 300) allows the overall inversion performance to be discovered.

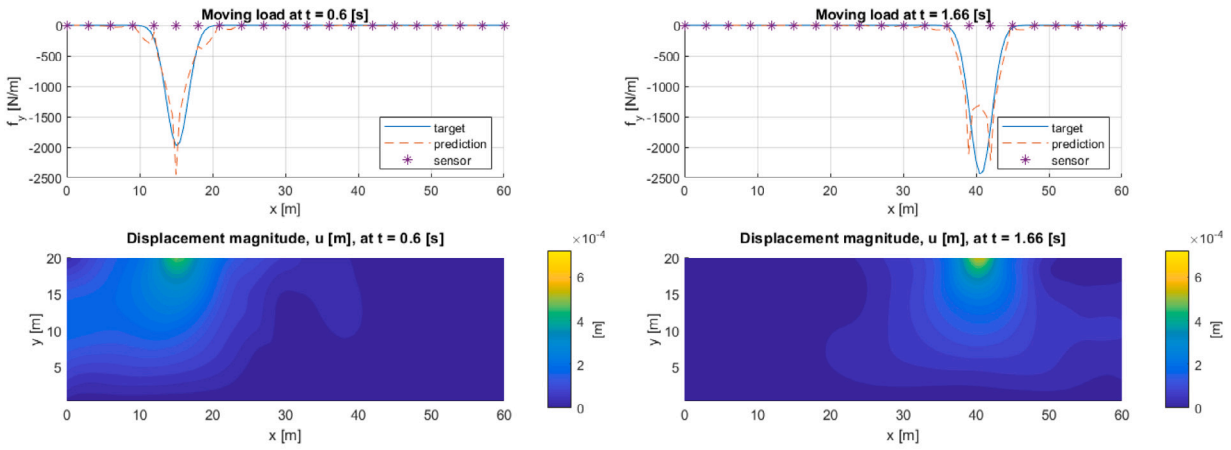

(a) (b)

Fig. 3. The snapshots of the target and predicted force distributions of a single moving wave source and the corresponding wave responses (displacement magnitudes) for the target loading at (a) $t = 0.6$ s and (b) $t = 1.66$ s for Case 1b.

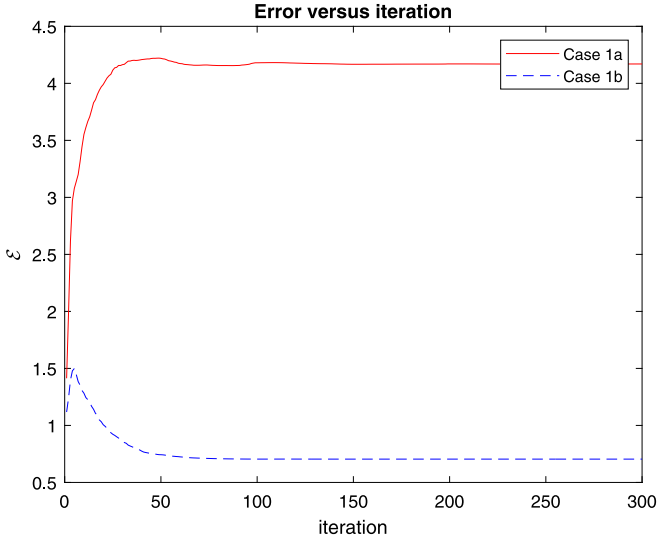

Fig. 4. Error over iteration for Example 1 up to 300 iterations: The guessed force is updated at every node in the domain in Case 1a versus at nodes only along the top surface in Case 1b. Updating guesses only along the top surface improves the performance of the inverse modeling.

and Case 1b estimate small x-components of the moving load as there is zero force in the x-direction for the target. Since it is reasonable to consider that any moving load in the presented problem must be located somewhere along the top surface, the method of updating the guessed loads only at the top surface is used for all following example cases.

Figs. 3(a) and 3(b) show the predicted and target vertical loading on the top surface as a function of x after 300 iterations for Case 1b at two time steps. Fig. 3 shows that the width and location of the moving dynamic distributed load are predicted well at both of the selected time steps. However, in Fig. 3(a), which shows a point in time in which the central peak of the load is located very near to a sensor location, the magnitude of the central peak amplitude is overestimated. Whereas, in Fig. 3(b), which show another point in time in which the central peak of the load is located nearly midway between to sensor locations, the magnitude of the peak amplitude is underestimated. Fig. 6 shows the target and predicted vertical load as a function of time at two locations on the for Case 1b after 300 iterations. Fig. 6(a) shows the predicted

Table 1
The properties of materials used in Examples 2, 3 and 4.

Layer	E (MPa)	ρ (kg/m^3)	ν	α (kg/(m^3 s))
Layer 1	15	1,600	0.2	25,000
Layer 2	25	2,400	0.3	12,500
Layer 3	45	2,000	0.25	37,500

and target f_y as a function of time at a point on the top surface, $(30, 20)$ m, where a sensor is located. Fig. 6(b) shows the predicted and target f_y as a function of time at a point on the top surface, $(31.5, 20)$ m, that is a meter and half away from the nearest senors, which are located at $(30, 20)$ m and $(33, 20)$ m. For both locations in Fig. 6, the timing of the load is predicted well. However, the magnitude of the load is overestimated at the sensor location and underestimated at a location away from the sensor. This reflects a tendency for the reconstruction to place more of the load at the sensor points than other points, which can be seen in Figs. 3 and 5.

5.2. Example 2: Effects of material complexity, sensor spacing, and load width on reconstructing moving surface loads

In Example 2, the solid consists of three materials in horizontal layers with Layer 1 at the top ($y = 15$ m to $y = 20$ m), Layer 2 in the middle ($y = 5$ m to $y = 15$ m), and layer 3 at the bottom ($y = 0$ to $y = 5$ m). The material properties used for these layers are listed in Table 1 and represent multi-layered ground soil . This example investigates the effects of material complexity, sensor spacing, and load width on reconstructing moving surface loads by studying the inversion performance in the following cases.

- Case 2a: The target loading in Case 2a is the same as the target loading in Example 1. The sensor spacing is one sensor every three meters for Case 2a (as in Example 1). However, the material properties in the domain under Case 2a, as mentioned above, are heterogeneous as opposed to Example 1. By comparing Case 2a with Case 1b, the effect of material heterogeneity on the inversion accuracy is examined.
- Case 2b: The conditions under Case 2b are identical to those of Case 2a except that the sensor spacing is reduced to one sensor every one and a half meters in Case 2b from one sensor every three meters in Case 2a. By comparing Case 2b with Case 2a, the effect of sensor spacing interval on inversion accuracy is investigated.

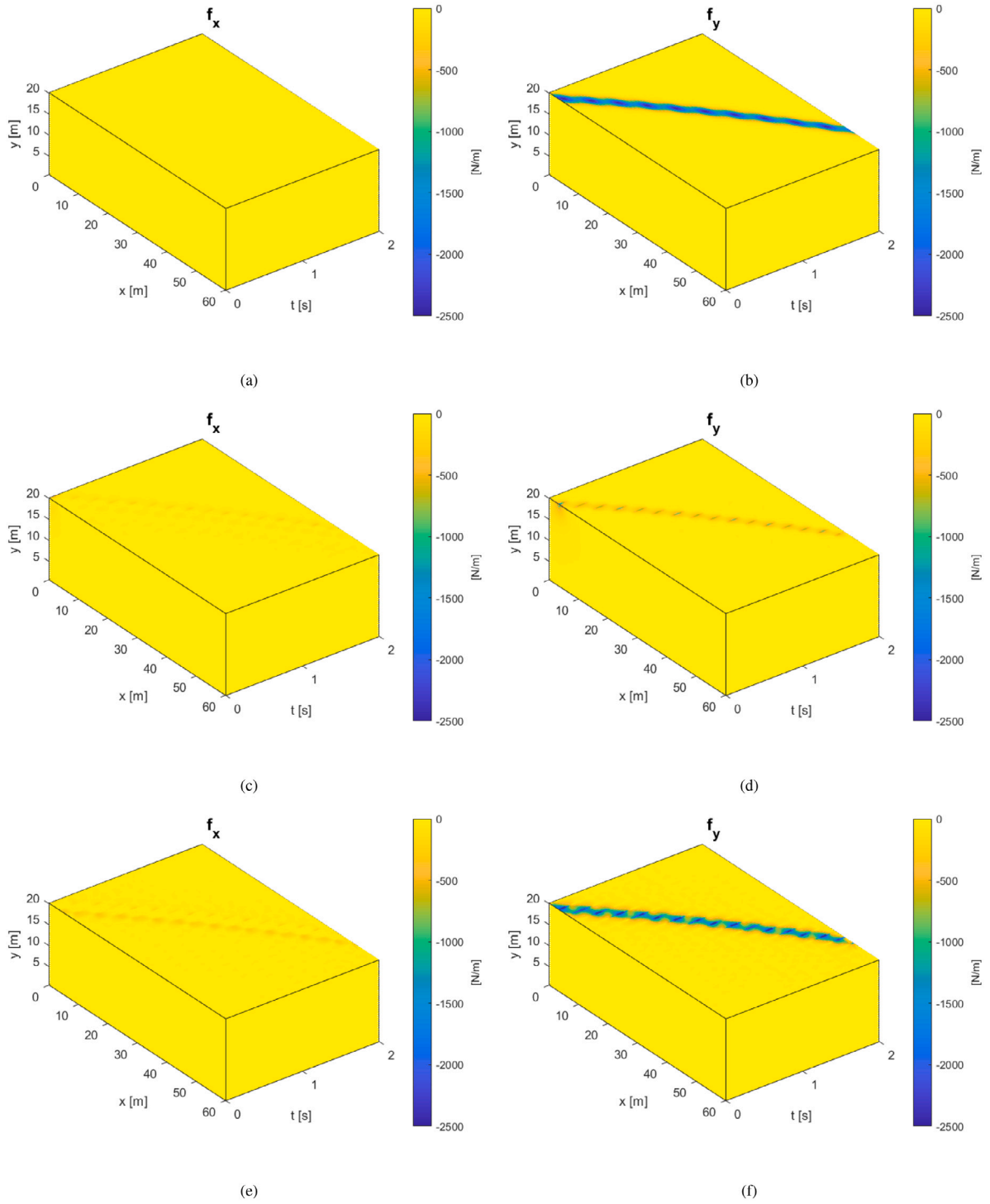

Fig. 5. Force in space and time for the 2D solid in Example 1 where (a) shows the target loading in the x-direction; (b) shows target loading in the y-direction; (c) and (d) show the reconstructed loading in x and y respectively after 300 iterations for Case 1a; (e) and (f) show the reconstructed loading in x and y respectively after 300 iterations for Case 1b.

- Case 2c: The conditions under Case 2c are identical to those of Case 2a except that the target loading in Case 2c has a narrower load-distribution width, $d = 0.75$ m (FWTM = 3.22 m), than its counterpart $d = 1.50$ m (FWTM = 6.44 m) in Case 2a. By comparing Case 2c with Case 2a, the relation between a load-distribution width and the inversion accuracy is studied.
- Case 2d: The conditions under Case 2d are identical to those of Case 2b except that the target loading in Case 2d has a narrower distribution width, $d = 0.75$ m (FWTM = 3.22 m) than its counterpart $d = 1.50$ m (FWTM = 6.44 m) in Case 2b. By comparing Case 2d with Case 2b and 2c, the effect of both the load-distribution width and sensor spacing on the inversion accuracy is investigated.

Simulations in this example show that reducing the distance between sensors improves the performance of the inversion as shown by the plots of the errors vs. iteration in Fig. 7. Namely, Case 2b achieves better accuracy than Case 2a with the same load distribution width for

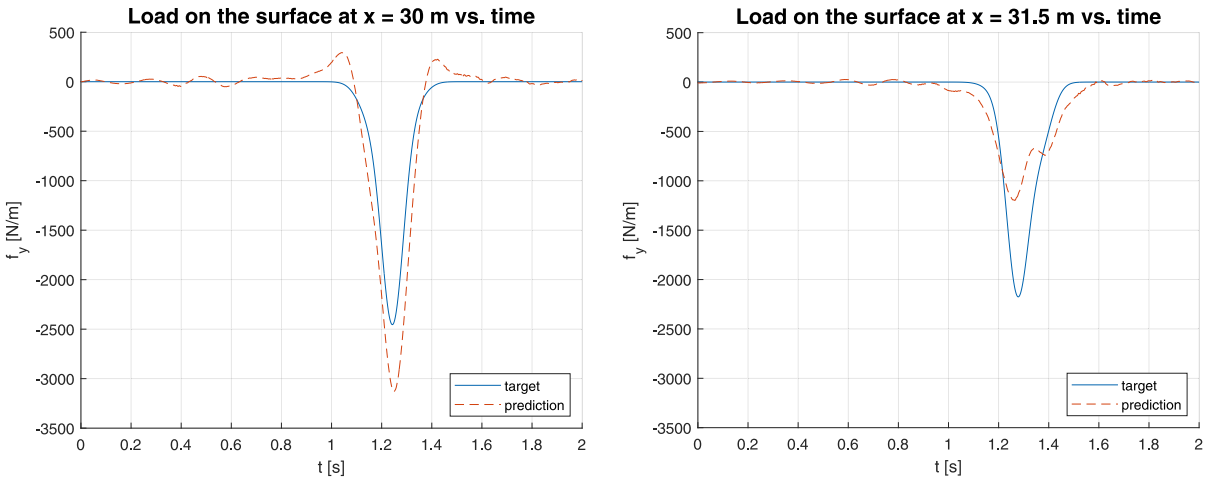

Fig. 6. The target and predicted y-component of force vs.time on the top surface of the 2D solid at (a) a sensor location (x = 30 m) and (b) midway between two sensors (x = 31.5 m) for Case 1b.

the target but having reduced sensor spacing, and, similarly, Case 2d achieves better accuracy than Case 2c with the same load distribution width for the target but reduced sensor spacing. However, reducing the width of the target load leads to less accurate inversion results. Namely, Case 2a achieves better accuracy than Case 2c, which is simulated at the same sensor spacing but with a wider distribution for the target load. Case 2b achieves better accuracy than Case 2d, which is simulated at the same sensor spacing but with a wider distribution for the target load. While the wider target load leads to a larger denominator in the normalized error plotted in Fig. 7, the error is smaller for wider loads even when this is accounted for. The finding from Example 2—the reconstruction of moving loads achieves better accuracy for wider distributed target loads and more densely spaced sensors—is consistent with results found for the 1D example cases studied by Lloyd and Jeong [42].

The target loading and sensor spacing in Case 2a are the same as in Case 1b. However, the solid in Case 2a is layered with three materials, and the solid in Case 1b consists of one material. Fig. 7 shows that the inversion for Case 2a, considering a solid with three horizontally layered materials, is nearly as effective as it is for the single-material solid considered in Case 1b.

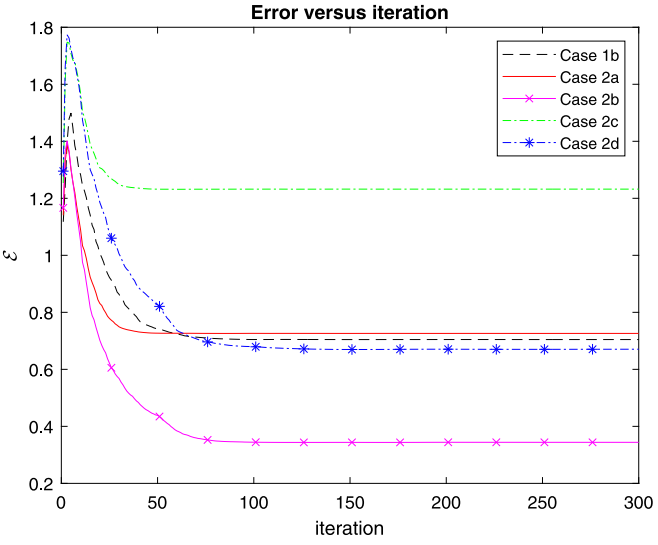

Fig. 7. Error vs. iteration for Example 2 up to 300 iterations: The performance of the inversion improves with denser sensor spacing and for loads with wider distributions. Case 2a: spacing = 3 m, FWTM = 6.44 m. Case 2b: spacing = 1.5 m, FWTM = 6.44 m. Case 2c: spacing = 3 m, FWTM = 3.22 m. Case 2d: spacing = 1.5 m, FWTM = 3.22 m.

5.3. Example 3: Multiple moving loads with both horizontal and vertical components of traction

In Example 3, the authors' inversion method is tested for multiple moving loads with x- and y-components of forces. This setting reflects that typical traction from vehicle wheels consists of both horizontal and vertical components. The material properties and layer geometries in Example 3 are the same as those (i.e., the 3-layered solid) in Example 2. In Example 3, three targeted moving loads with vertical and horizontal components of force (Loads A, B, and C) are simultaneously applied to the top surface of the solid. The vertical and horizontal components of each load have a spatial distribution, which varies over time, along the top surface where the FWTM of each load is 3.22 m. The horizontal loading for each moving load has the same central peak position and width as the corresponding vertical loading.

- Load A: The amplitude of vertical force for Load A is $P_y(t)_1 = -[500\sin(2\pi(15)t)+2000]$ N/m. The horizontal component of Load A has an amplitude of $P_x(t)_1 = -[500\sin(2\pi(15)t)+1034+1.225(20+3.6t)^2]$ N/m. The x-location of the central peak for both the vertical and horizontal loadings for Load A is $b(t)_1 = [2.5 + 20t + 0.5(3.6)t^2]$ m.
- Load B: Load B has a vertical force amplitude $P_y(t)_2 = -[500\sin(2\pi(10)t)+2000]$ N/m and a horizontal force amplitude $P_x(t)_2 = -[500\sin(2\pi(10)t)-1168+1.225(30-7.2t)^2]$ N/m. Both of them have the same central peak location $b(t)_2 = [-10 + 30t - 0.5(7.2)t^2]$ m.
- Load C: Load C has a vertical force amplitude $P_y(t)_3 = -[500\sin(2\pi(5)t) + 2000]$ N/m and a horizontal force amplitude $P_x(t)_3 = -[500\sin(2\pi(5)t) - 1066]$ N/m. Both of them have the same central peak location $b(t)_3 = [45 - 25t]$ m.

Fig. 8 shows snapshots of the three moving loads in Example 3 and the resulting displacements at two points in time. All of the vertical components of the target loads in Example 3 act in the negative y-direction throughout the observation period. However, Loads B and C

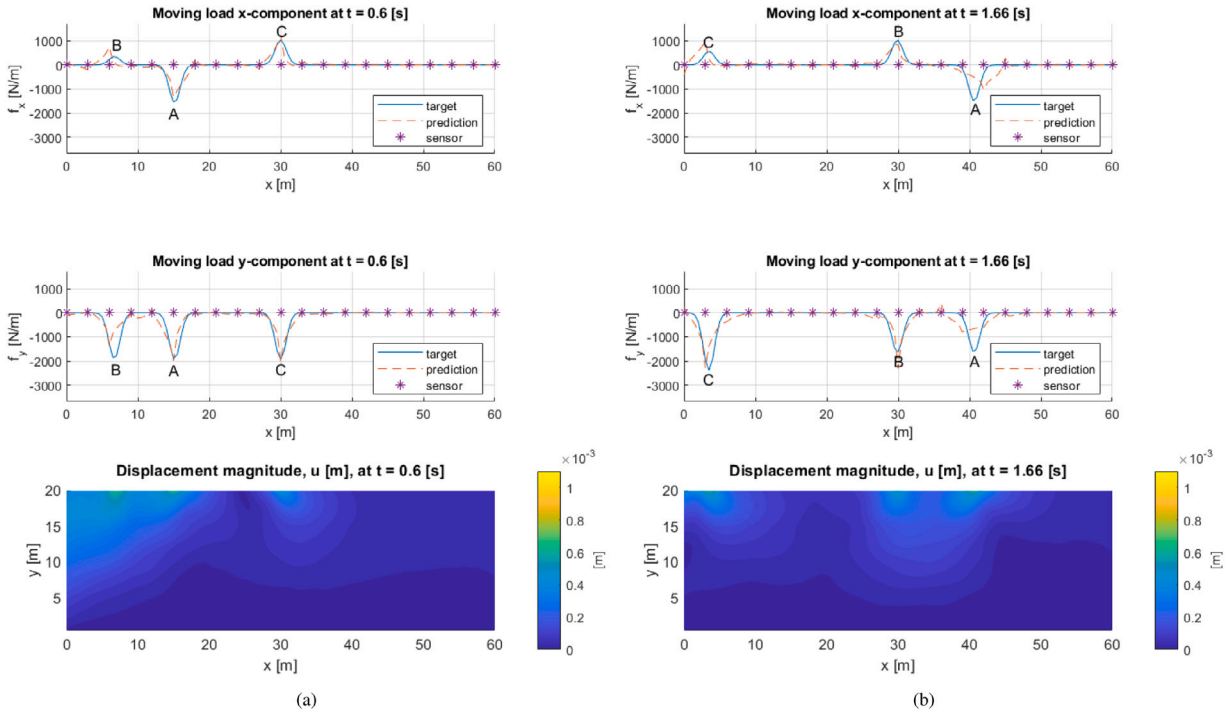

Fig. 8. The snapshots of the target and predicted force distributions of three moving wave sources and wave responses (displacement magnitudes) for the target loading at (a) $t = 0.6$ s and (b) $t = 1.66$ s for three loads (A, B, and C) in Example 3.

have positive horizontal components of force, while Load A has only a negative horizontal component of force. The first part of the horizontal load, like the dynamic part of the vertical load, uses a sine function and does not represent any specific dynamic load. The second part uses $ma \pm \left(C_r mg + D_a v^2\right)$, which represents the frictional force acting on top surface of the solid assuming the surface is flat. The terms $C_r mg$ and $D_a v^2$ can be used for representing the rolling resistance and the wind drag respectively, and their signs should be opposite the sign of the velocity of the moving load, v. Hypothetical but reasonable numbers were chosen for the coefficients C_r and D_a. The second part is also time varying since it can consider the velocity of the moving load varies with time. However, like for the vertical load components, 6.44 m and 3.22 m are not realistic widths of surface contact. Fig. 9 shows the contour plots of the target and the reconstructed loads after 300 iterations in Example 3. Fig. 9 shows that the presented algorithm to reconstruct the loading profile accurately estimates the number of moving loads and their moving directions as well as time-dependent locations. The general positions of the reconstructed moving loads match their targets well.

5.4. Example 4: Reconstructing moving loads with horizontal and vertical components of traction using sensors measuring only vertical displacements

The setting in Example 4 is the same as that in Example 3 except that, while the sensors in Example 3 measured displacements in the x- and y-directions, the sensors in Example 4 only measure vertical displacements. Fig. 10 shows that, for force in the y-direction, the reconstructed loads in Example 4 after 300 iterations are similar to the reconstructed loads in Example 3 after 300 iterations. However, for force in the x-direction, the accuracy of reconstructing loads is lower in Example 4 than in Example 3. Fig. 11(a) shows the error at each iteration for Examples 3 and 4 up to the 300th iteration. Figs. 11(b) and 11(c) show the error for the x- and y- components of force, respectively, for Examples 3 and 4 at each iteration up to the 300th iteration. The normalized mean absolute errors for the x- and y- components of force are computed as follows:

$$\varepsilon_x = \frac{\frac{1}{N_p}\sum_{i=1}^{N_i}\sum_{j=1}^{N_j}\left|f_{x_{ij_{\text{target}}}} - f_{x_{ij_{\text{estimate}}}}\right|}{\frac{1}{N_p}\sum_{i=1}^{N_i}\sum_{j=1}^{N_j}\left|f_{x_{ij_{\text{target}}}}\right|} \quad \text{and}$$
$$\varepsilon_y = \frac{\frac{1}{N_p}\sum_{i=1}^{N_i}\sum_{j=1}^{N_j}\left|f_{y_{ij_{\text{target}}}} - f_{y_{ij_{\text{estimate}}}}\right|}{\frac{1}{N_p}\sum_{i=1}^{N_i}\sum_{j=1}^{N_j}\left|f_{y_{ij_{\text{target}}}}\right|} \tag{44}$$

where N_i is the number of points in time, N_j is the number of points in space, and N_p is the total number of points in space and time. The error plots in Fig. 11 show that the inversion performs better in Example 3 which has sensors measuring displacements in both x- and y-directions than in Example 4 which has sensors measuring displacements in only the y-direction. However, Figs. 11(b) and 11(c) show that the most significant increase in error for Example 4 as compared to Example 3 occurs in the estimation of the loading in the x-direction, i.e., the direction in which displacements are not measured in Example 4. For Example 4, The accuracy of the inversion for the y-component of force is significantly better than it is for the x-component of force.

6. Experimental validation of stationary-source inversion

The presented source inversion algorithm is validated by using experimental data. The experimental data on a real-scale roadway induced by moving vehicle traction is not suitable to be utilized as input data in the presented inverse modeling yet because the authors' wave model is based on a bounded 2D domain (it will be extended to an unbounded 3D domain in the future). To bridge this gap for the experimental validation, experimental data from a bounded solid in the laboratory is used. Since the scale of the lab specimen is small (e.g., the order of magnitude of the domain size is 10 cm by 10 cm), experimental data of a very high-frequency range (e.g., the order of magnitude of 100 kHz) is obtained. Under such a high-frequency excitation, transducers suffer from low sensitivity so that it is not feasible to implement a "moving" wave source. Instead, a non-moving wave source is used

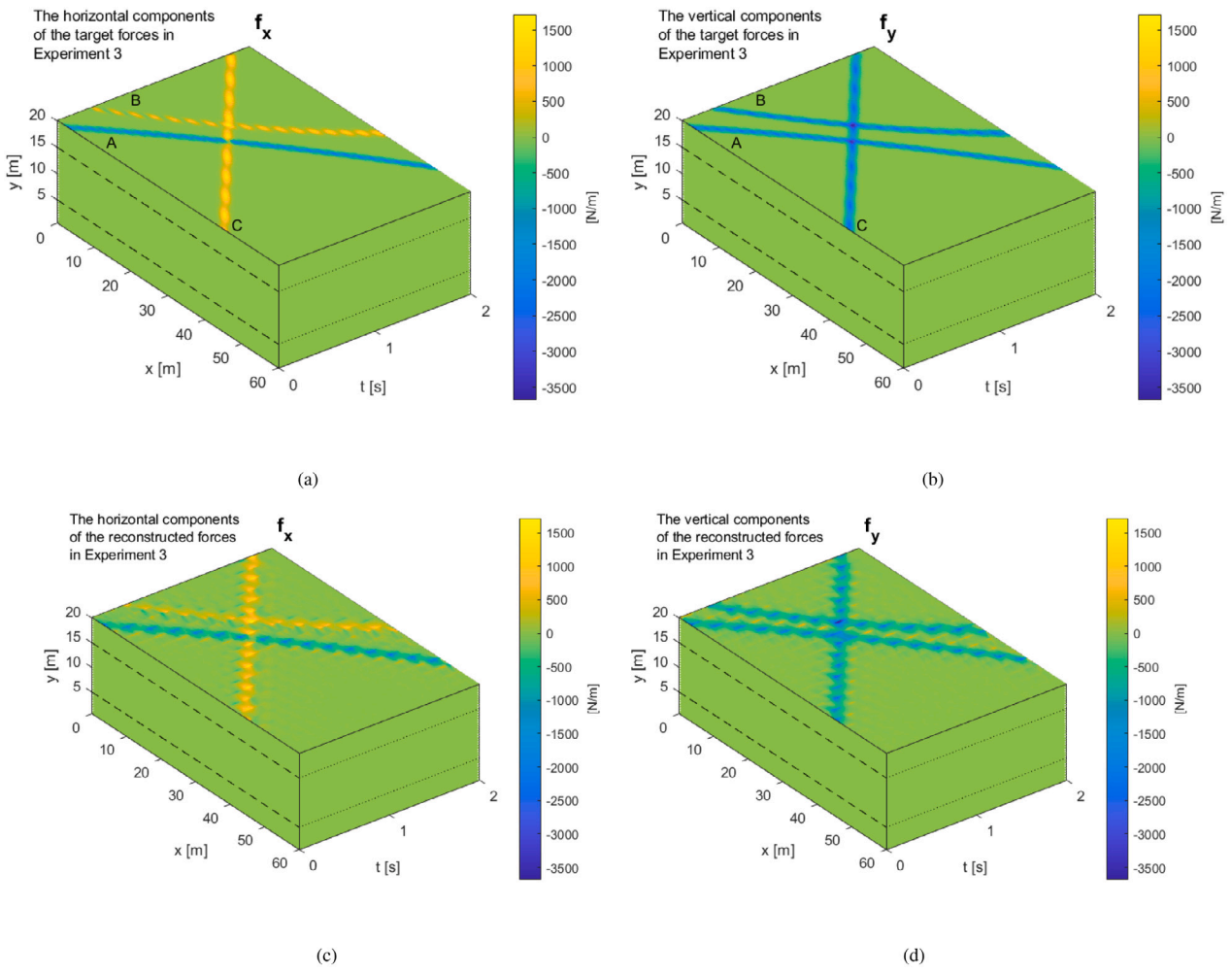

Fig. 9. Force in space and time for the 2D solid in Example 3 where (a) shows the target loading in the x-direction; (b) shows target loading in the y-direction, (c), and (d) show the reconstructed loading in x and y after 300 iterations.

in the experiment. Using the test data from the stationary source, our source-inversion modeling code is utilized to identify the temporal and spatial distribution of the wave source on the top of the solid.

6.1. Experimental setup

As shown in Fig. 12, two ultrasound contact transducers (Digitalwave B-454) are arranged in a pitch–catch configuration on the top surface of the specimen. Ultrasound gel is applied between the transducers and the specimen, and a weight is placed on top of the transducers to help achieve consistent contact conditions even in the presence of uneven surface roughness. Positioning is aided through a 3D-printed template that is only in contact with the substrate at its corners. A 20-cycle sinusoidal Hann-windowed tone burst at $f = 100$ kHz is generated by an arbitrary waveform generator (Keysight 33512B) and directly fed into the actuator. To record the measurements, the sensing transducer is connected to the oscilloscope (PicoScope 5442D). Signals are recorded for up to 1.0 ms with a sampling rate of 125 MHz. In order to improve the signal-to-noise ratio of the measurements, the analyzed signal is the time-average of 200 repeated acquisitions.

The studied test object is a 199.44 mm (L) × 150.04 mm (H) × 15.85 mm (D) 6061 aluminum block. It rests on a soft cloth to isolate it from the experimentation table and is held upright through the use of a C-clamp as shown in Fig. 12(a). It should be noted that different (isolated) mounting options are evaluated without observing any significant differences in the signals, thus confirming that nearly "free-free" boundary conditions are established. The employed template allows for the transducer to be located every 10 mm, starting from the origin on the left. The actuator (~19 mm diameter) is placed at the stationary location of $x_a = 70$ mm. The roving sensor is placed at every other possible location in subsequent experiments, i.e., at $x_s \in [10, 30]$ mm and $x_s \in [110, 180]$ mm. Namely, the experiments are repeated with the sensor being placed at various locations to mimic having a grid of sensors at the corresponding positions. This is a commonly used practice when not enough sensors are available at a time: in this work, eleven sensors should be employed for experimental validation so that one-sensor measurement was repeated eleven times. Fig. 12(b) shows a typical raw signal of a measured dynamic response with the receiver at $x_s = 160$ mm. The larger amplitude of the measured signal at the receiver at the time after 200 us is attributed to reflection.

6.2. Simulation setup

To simulate the physical validation experiments, a 2D plane stress FEM model of the aluminum plate is used rather than the plane strain model used for Simulations 1 through 4. A plane stress model is used because the thickness of the aluminum plate, or the z-direction dimension of the plate, is much smaller than the dimensions of the plate in the x- and y-directions, and the plate is mostly unconstrained in the z-direction. The 2D model of the aluminum plate matches the dimensions of the laboratory specimen, i.e., it has a length of $L = 0.200$ m, a height

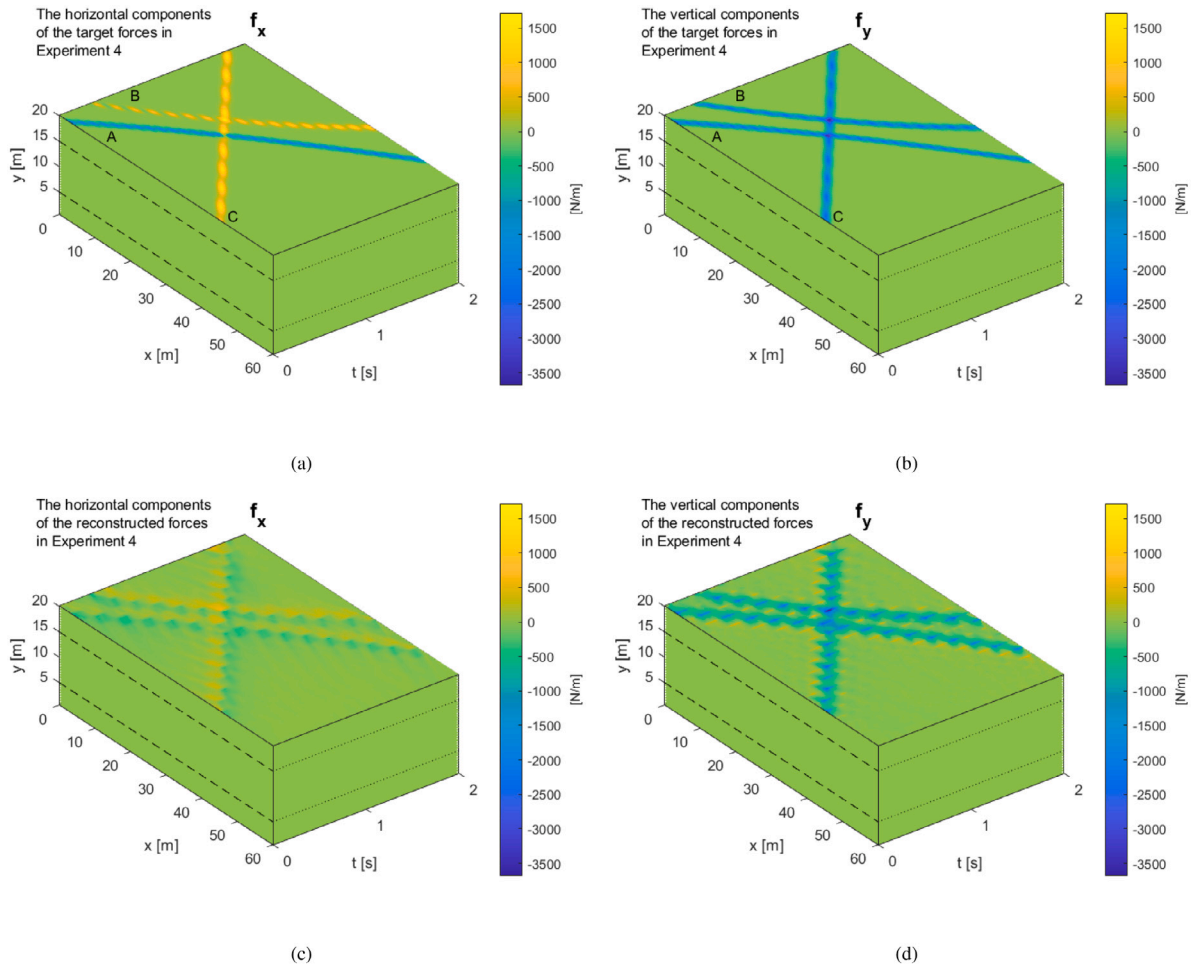

Fig. 10. Force in space and time for the 2D solid in Example 4 where (a) shows the target loading in the x-direction; (b) shows target loading in the y-direction, (c), and (d) show the reconstructed loading in x and y after 300 iterations.

of $H = 0.150$ m, and a constant thickness of 0.01585 m. The 2D plane-stress FEM model consists of nine-node elements of the uniform size 0.005 m × 0.005 m. For the simulations of the aluminum plate, the material properties of $E = 68.9$ GPa, $\rho = 2700$ kg/m^3, $\nu = 0.33$, and zero damping are used. The boundary and initial conditions are the same as described in Section 2 (i.e., fixed bottom boundary and zero initial value conditions). The observation time is $T = 2 \times 10^{-4}$ s, and the time step size is $\Delta t = 4 \times 10^{-7}$ s. In the experimental setup, there is a gap in the sensor locations between $x = 0.030$ m and $x = 0.110$ m to avoid mechanical interference with the actuator at $x_a = 0.070$ m. Accordingly, these approximate width and location of the load are considered to have been estimated prior to the inversion. In addition, it is assumed that the actuator only applies normal forces (y-direction) to the surface, as the low-viscosity ultrasound gel used does not allow for shear force transmission. Similarly, the receiver is assumed to only measure displacements normal to the surface.

6.3. Inversion simulation of a pseudo experiment using synthetic measurement created by a synthetic target with the Gaussian spatial distribution

Before using the presented inversion method to reconstruct the experimental loading profile with data from the sensors used in the physical experiments, numerical (pseudo) experiments with synthetic sensor data are conducted. First, displacement fields of wave responses are generated using an FEM simulation, in which a stationary, 20 mm-wide Gaussian-distributed targeted dynamic load is applied. The center of its spatial Gaussian distribution is located at the center point ($x_a = 70$ mm) of the actuator in the physical experiment. Considering the raw signal at the transducer (i.e., loading data) from the physical experiment to be a force in Newtons, the synthetic target distributed load (in the unit of Newtons per meter) is designed such that the magnitude of its spatially-integrated force signal is equal to the magnitude of the experimental force signal at each time step. The width of the synthetic targeted distributed load is set to approximate the width of the transducer. However, it is hypothetical that the type of the spatial distribution of the synthetic target load is Gaussian.

In this simulation, y-direction displacements generated by the forward simulation, due to the targeted synthetic load, at sensor locations are the measured data for the inversion. Note that the physical experiments mainly provide measurements in the y-direction. In addition, only y-direction forces, with vanishing x-direction force, between $x = 0.060$ m and $x = 0.080$ m on the top surface of the plate are updated each iteration. Namely, the amplitude of the stationary targeted load—how the amplitude varies with time and how the load is spatially distributed at each time step—is updated. The inversion result after 300 iterations matches the target loading as Fig. 13 shows. This simulation indicates that the presented inversion simulation can generally identify the unknown distribution over space and time of synthetic traction in this high-frequency setting.

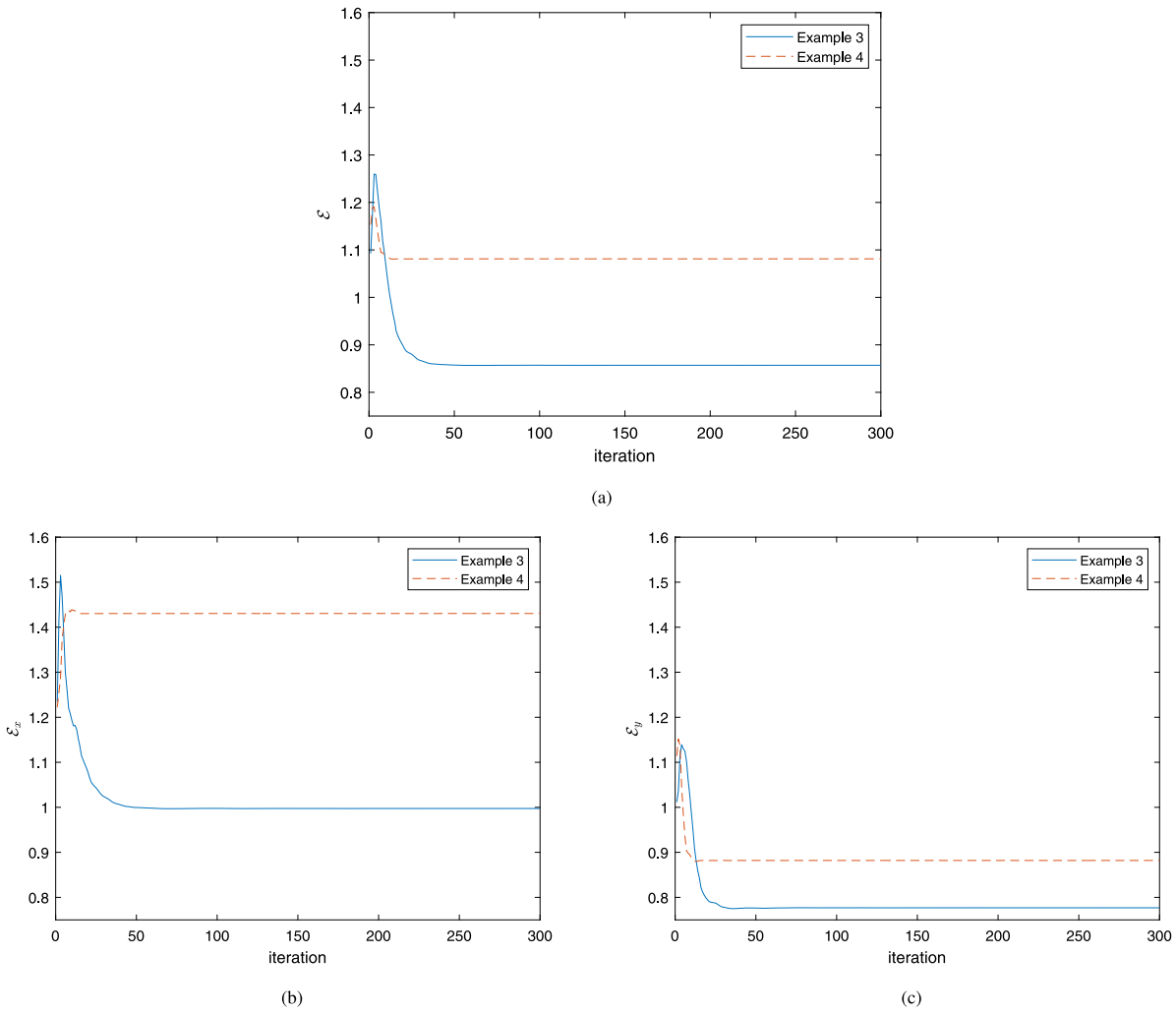

Fig. 11. Error for Examples 3 and 4 (a) shows the error at every iteration up to the 300th iteration; (b) shows the error for the x-component of force at every iteration up to the 300th iteration; (c) shows the error for the y-component of force at every iteration up to the 300th iteration.

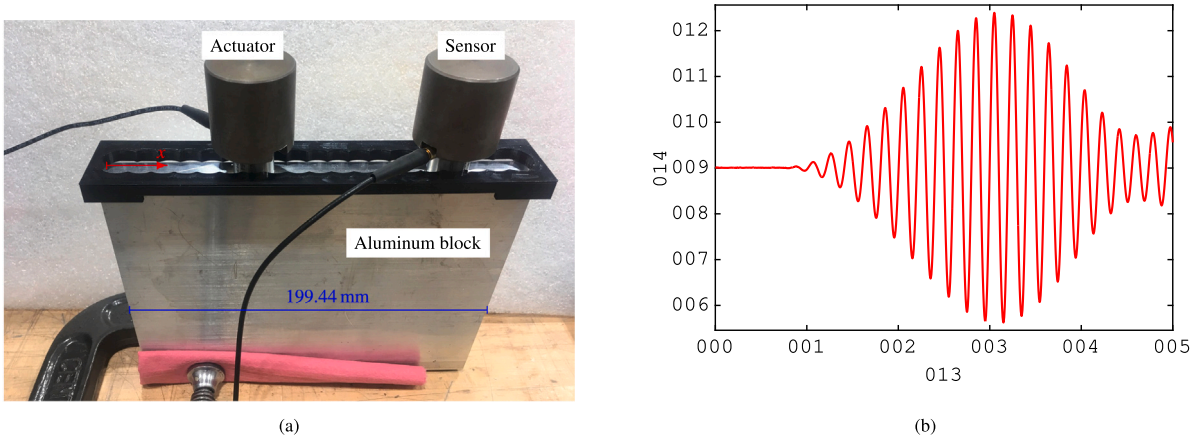

Fig. 12. Laboratory setup for high-frequency, validation experiments where (a) shows contact transducers positioned via template on top of "free-free" aluminum block and (b) shows a typical raw signal for $x_a = 70\,\text{mm}$ and $x_s = 160\,\text{mm}$.

Comparisons between the real measured displacements and their synthetic counterparts, induced by this synthetic target load, are shown for a few selected sensor locations in Fig. 14. While there are similarities between the measured displacements and the displacements computed for the synthetic loading, the differences between the measured and synthetic displacements suggest in part that the actual spatial distribution of the load is different from the hypothetical Gaussian distribution used for the synthetic load, in addition to other effects that are present during the experiments such as transducer ringing.

In summary, this pseudo experiment shows that the presented inversion scheme is able to accurately identify a targeted load of which spatial distribution is assumed to be the Gaussian distribution (as

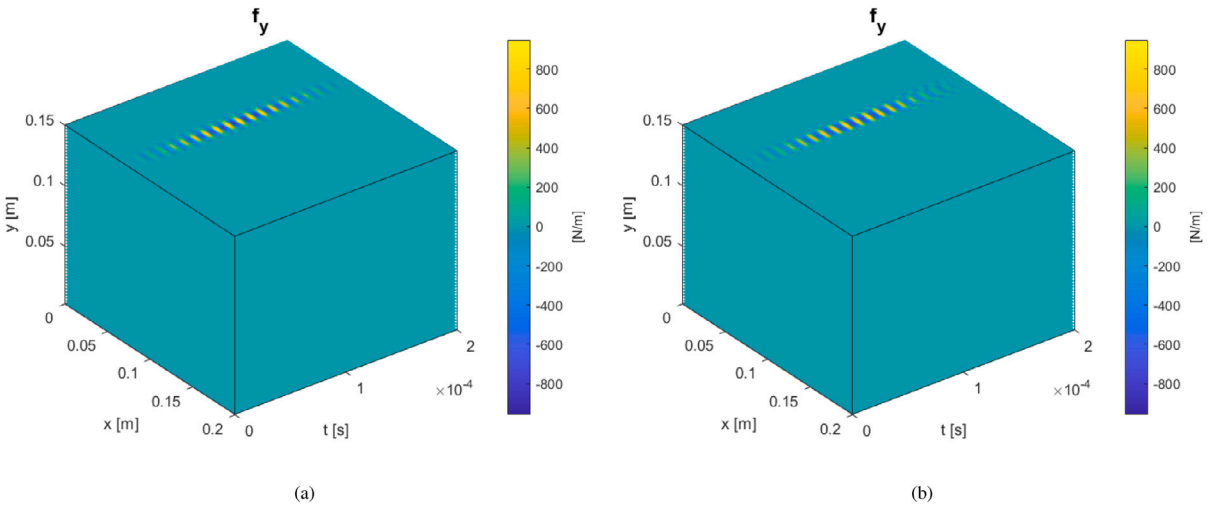

Fig. 13. Inversion results using synthetic measurement data in a lab-scale domain; (a) shows the target loading; (b) shows the reconstructed loading after 300 iterations.

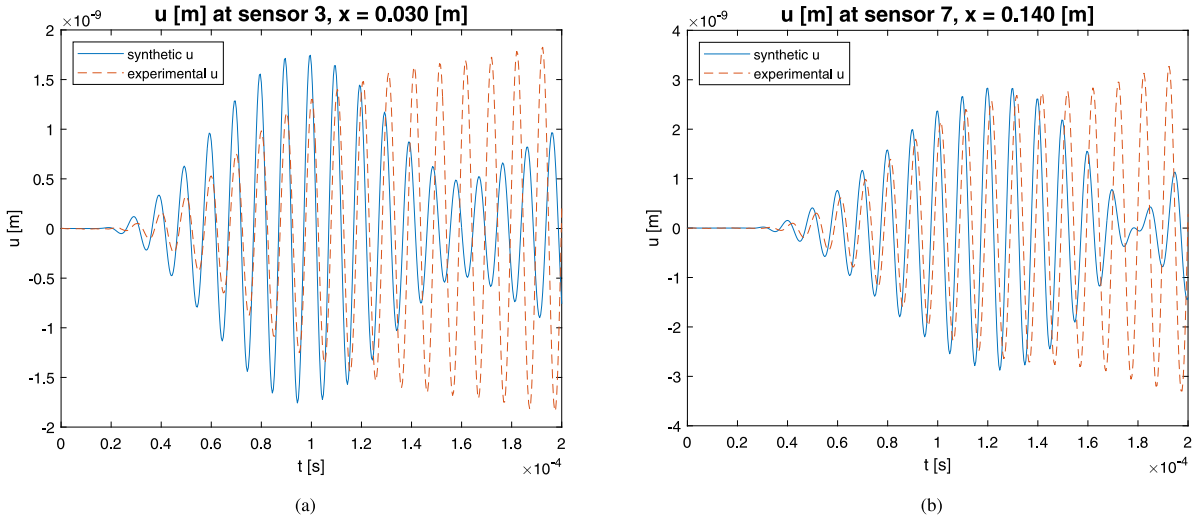

Fig. 14. Comparisons of experimental measurements of displacements and synthetic counterparts computed using FEM and the synthetic loading hypothesized as a Gaussian distributed load at 2 out of 11 sensor locations.

shown in Fig. 13). In addition, the wave responses at the sensor locations, by this synthetic target load, mismatch those by the real target load (as shown in Fig. 14), meaning that the spatial distribution of the latter may not be Gaussian. Namely, the validation of the inversion method using real experimental measurement, shown in the next subsection, may disclose the unknown spatial distribution of a real, experimental targeted load.

6.4. Inversion simulation using real experimental measurement

In the inversion simulations using experimental measurements, the objective and Lagrangian functionals utilize displacement measurements obtained by physical experiment (sensor data from 11 locations multiplied by the time step for the raw data, $\Delta t_{\text{data}} = 8 \times 10^{-9}$ s).

6.4.1. Validation of inversion using a larger observation time (2×10^{-4} s)

Fig. 15 shows the inversion results based on the measured displacements after 300 iterations. The targeted spatial distribution of the load in the experiment is unknown, so the spatial distribution of the reconstructed load cannot be directly compared to that of the actual load. Rather, in this example, the time signal of the spatially-integrated magnitude of the reconstructed load is compared to the magnitude of the experimental load signal as shown in Fig. 15(b), which shows that the mismatch between the former and the latter increases most notably at the later portion of the total observation period. Figs. 15(c) and 15(d) show comparisons of the measured displacements and FEM computed counterparts based on the reconstructed loading for two of the eleven sensor locations. The computed responses, due to the inverted load, in Figs. 15(c) and 15(d) are much closer to the measured responses than their counterparts, induced by the aforementioned hypothetical synthetic load, in Fig. 14. However, the measured wave responses at the sensors are still not fully reconstructed by the inverted loading, and the authors' inversion solver is stalled at this result even beyond the 300th iteration. The noticeable mismatch between the two displacement in Fig. 15(c) suggests that the inversion solver is trapped in a local minimum that is not even close to the global minimum. The authors suggest that the inversion result in the simulation in this Section 6.4.1 is not correct primarily because of the following reason.

The bottom boundary condition of the FEM model does not completely replicate its real counterpart in the experiment, which suggests that waves that reflect off of the bottom boundary and reach the sensors during the observation period of the experiment may cause inaccuracies in the inversion result. Namely, for the plate used in the experiment, the wave speed for P-waves is $v_p = 6149$ m/s and the wave speed for

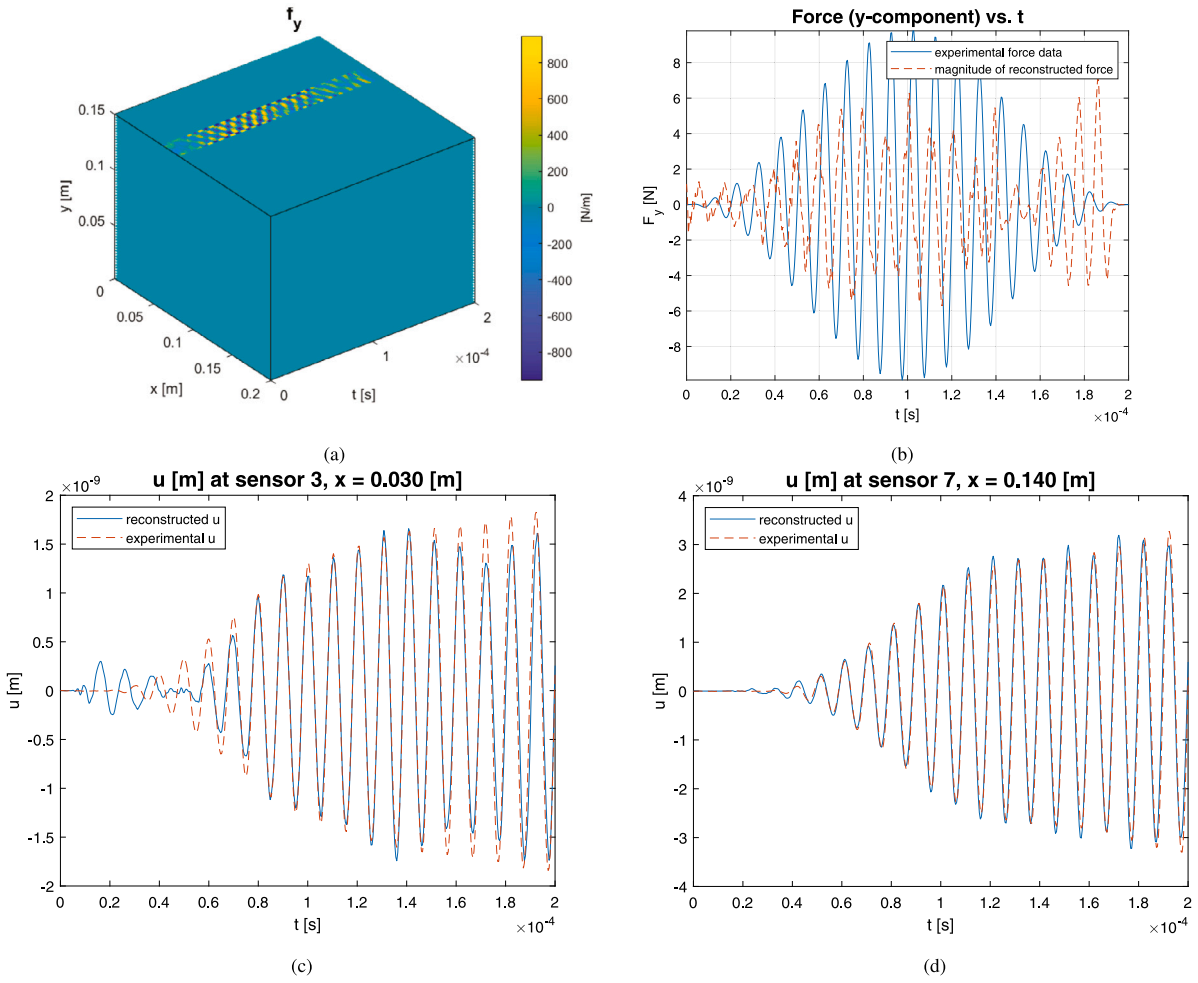

Fig. 15. Inversion results for the 2D Aluminum plate model using experimental measurements updating only y-directed forces on the top surface between $x = 0.060$ m and $x = 0.080$ m; (a) the reconstructed loading in N/m in the y-direction at the 300th iteration; (b) the spatially-integrated reconstructed force and the experimental force vs. time at the 300th iterations; (c) and (d) shows comparisons, at 2 out of 11 sensor locations, between experimental measurements of displacements and those computed with FEM using the reconstructed loading from the 300th inversion iteration.

S-waves is $v_s = 3097$ m/s. P-waves traveling from the top of the plate, where the loading is applied, take 4.88×10^{-5} s (about 25% of the total observation period) to travel from the top, reflect off of the bottom, and return to the top of the plate; and S-waves take 9.69×10^{-5} s (about 50% of the total observation period) to do the same.

6.4.2. Validation of inversion using a shorter observation time (9×10^{-5} s) *to limit the impact of the strong reflected S-waves from the bottom*

To limit the impact of the strong reflected S-waves on the inversion, the inversion procedure is conducted for an observation period of 9×10^{-5} s (about 45% of the total observation period). Even using the short observation time for the validation does not exclude the reflection of P-wave from the bottom boundary, but its amplitude is smaller than that of S-wave. Fig. 16 shows the inversion results for this reduced observation time after 900 iterations. Fig. 16(b) shows the spatially-integrated magnitude of the reconstructed load in this example compared to the magnitude of the experimental load signal up to $t = 9 \times 10^{-5}$ s. Figs. 16(c) and 16(d) show comparisons of the measured displacements up to $t = 9 \times 10^{-5}$ s and FEM computed counterparts based on the reconstructed loading for the reduced observation time at two of the eleven sensor locations. The measured wave responses at the sensors are accurately reconstructed by the inverted loading, which suggests that the presented inversion algorithm can more effectively reconstruct the force signal at the actuator during the reduced observation than the full one. Fig. 16(e) shows the final-reconstructed distribution of the traction from the actuator over space and time. It shows that the spatial distribution is not symmetric with respect to the centroid of the actuator, which suggests that such an asymmetric loading may be attributed to the (unknown) internal structural dynamics of the off-the-shelf actuator.

6.5. The limitation of the presented experiment for validating moving wave-source inversion

Even though a moving source test could not be implemented as part of this study, the general feasibility of the inversion method is shown in the presence of measurement noise and other non-ideal conditions such as positional errors and inherent delays added by the measurement equipment. In the future, a moving source test could potentially be implemented through a low-frequency large-scale field test as high-frequency lab-scale testing would require very high velocities for the source to be noticeable within the short measurement frame.

7. Conclusion

The authors discuss the wave-source inversion method for the reconstruction of the temporal and spatial distributions of moving or stationary wave sources on the top surface of a two-dimensional (2D), heterogeneous, damped, linear elastic solid by using the vibrational

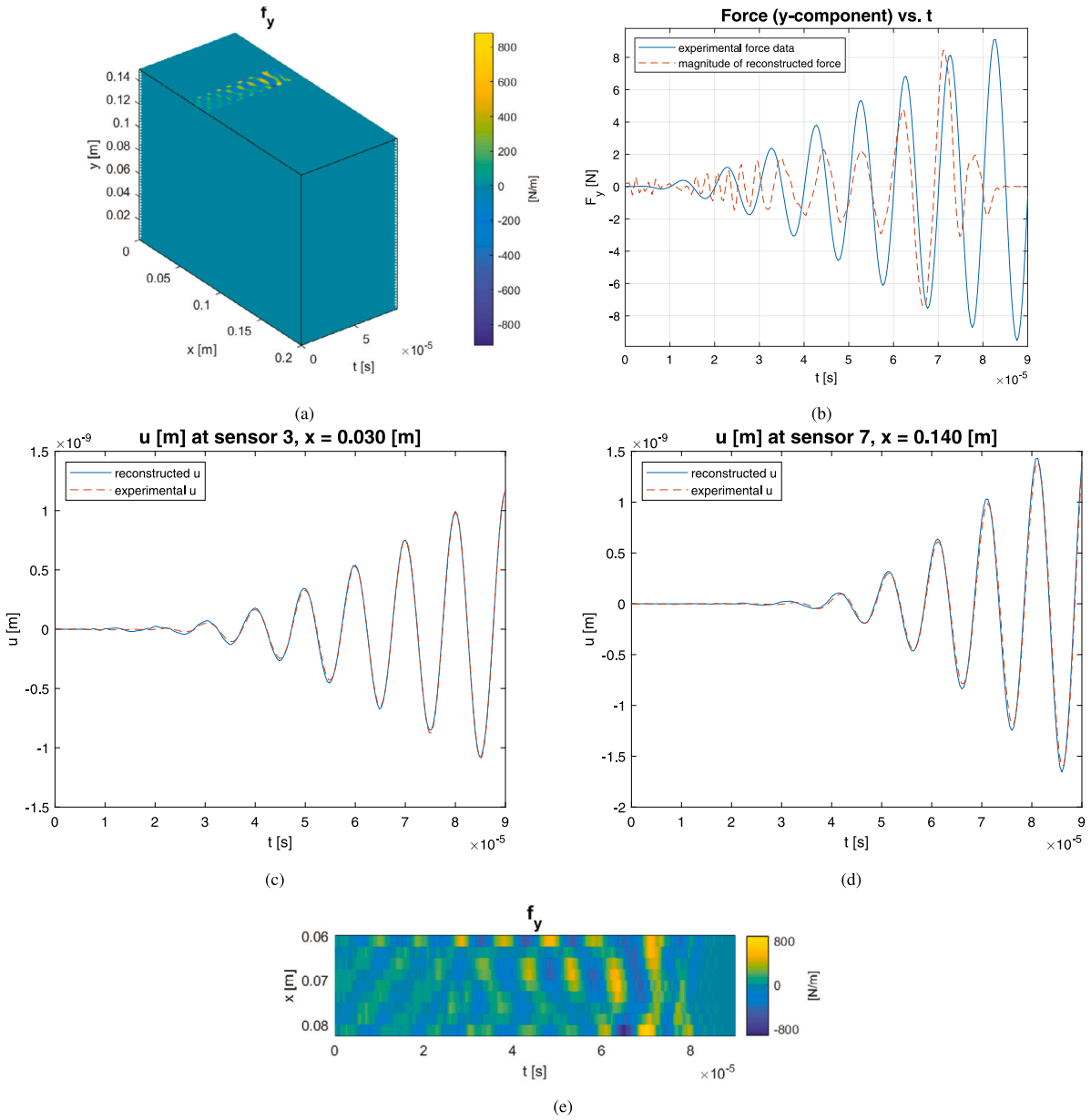

Fig. 16. Inversion results using experimental measurements up to $t = 9 \times 10^{-5}$ s after 900 iterations; (a) the reconstructed loading in N/m in the y-direction; (b) the spatially-integrated reconstructed force and the experimental force vs. time at the 900th iterations; (c) and (d) show comparisons, at 2 out of 11 sensor locations, between experimental measurements of displacements and those computed with FEM using the reconstructed loading at the 900th inversion iteration; (e) contour plot of the reconstructed loading at the top surface from $x = 0.06$ m to $x = 0.08$ m in N/m over time.

measurement from the top surface. The adjoint-gradient-based source inversion method is used within the context of DTO because of its compact formulation. The FEM is used for obtaining the solutions of state and adjoint wave problems.

The numerical experiments show that the presented wave-source inversion method is effective at reconstructing target moving or stationary wave sources along the surface of a 2D solid modeled using plane strain or plane stress formulations in FEM without prior knowledge about the loads. The inversions using the plane-strain formulation are carried out for numerical-only simulations in Section 5. Conversely, the inversions, easily switched to the plane-stress setting, are performed in Section 6 for the simulations that are validated by experiments. The following conclusions can be made based on the numerical experiments conducted for this study.

- The method of updating the guessed loading only at nodes along the top surface of solid performs better than updating the guess at every node in the entire domain of the FEM model.
- Reducing the distance between the sensors improves the accuracy of the inversion, while reducing the distribution widths for the target loads leads to less accurate results. Further investigation of the numerical experiment results, including the tendency to

underestimate the loads when they move to locations between sensors, could lead to improving results for more realistic sensor spacing to load width ratios for sparsely spaced sensors in future research.

- The inversion results for the presented case of a moving load on the top surface of a horizontally layered solid consisting of three different materials are nearly as accurate as inversion results for an identical moving load on a homogeneous solid.
- The inversion method presented is effective at reconstructing multiple loads with both x- and y- components of forces.
- The accuracy of identifying multiple moving wave sources by using sensors that measure both horizontal and vertical components of wave motions turns out to be greater than that using sensors measuring only vertical motions.
- The presented inversion method for a stationary wave source is validated for a limited observation time by using measurement data of wave motions in lab-scale experiments using high-frequency (100 kHz) excitation. The authors suggest, though, that more realistic modeling of the bottom boundary condition using a high-performance 3D wave solver (e.g., the spectral element method [45–48]) could potentially allow for the full observation time to be considered in the experimental validation.

While this paper investigates a numerical method to reconstruct the spatial and temporal profile of wave sources in a 2D heterogeneous solid, the wave-source inversion can be extended to a 3D setting. Thus, it can be utilized for practical applications of moving vibrational tractions in various environments (e.g., a 3D solid with a non-flat surface, such as hills; a solid where sources move in a non-straight fashion, such as a turn). In addition, the stationary wave-source inversion can be useful for detecting the stationary impact load in a complex-shaped 3D structure, for which other methodologies cannot be employed for source detection because of complex wave responses induced by reflection, refraction, and mode conversion. The computational challenge in a 3D bounded/unbounded domain can be addressed by using the spectral element method [45–48].

Declaration of competing interest

The authors declare that they have no known competing financial interests or personal relationships that could have appeared to influence the work reported in this paper.

Data availability

Some or all data, models, or code generated or used during the study are available from the corresponding author by request.

- MATLAB code (.m format) of the presented inverse modeling that contains the optimization solver and the forward and adjoint wave solvers.
- MATLAB datasets (.mat format) of the presented numerical results.

Acknowledgments

This material is based upon work supported by the National Science Foundation under Award CMMI-2044887 and CMMI-2053694. Any opinions, findings, and conclusions or recommendations expressed in this material are those of the authors and do not necessarily reflect the views of the National Science Foundation. The authors are also grateful for the support by the Faculty Research and Creative Endeavors (FRCE) Research Grant-48058 at Central Michigan University. The authors also greatly appreciate the reviewers' very constructive comments, which substantially helped improving the paper.

References

[1] T. Kundu, H. Nakatani, N. Takeda, Acoustic source localization in anisotropic plates, Ultrasonics 52 (6) (2012) 740–746.
[2] T. Kundu, Acoustic source localization, Ultrasonics 54 (1) (2014) 25–38.
[3] T. Kundu, S. Das, K.V. Jata, Point of impact prediction in isotropic and anisotropic plates from the acoustic emission data, J. Acoust. Soc. Am. 122 (4) (2007) 2057–2066.
[4] R. Unnthorsson, T.P. Runarsson, M.T. Jonsson, Acoustic emission based fatigue failure criterion for CFRP, Int. J. Fatigue 30 (1) (2008) 11–20.
[5] A. Carpinteri, G. Lacidogna, N. Pugno, Structural damage diagnosis and life-time assessment by acoustic emission monitoring, Eng. Fract. Mech. 74 (1) (2007) 273–289.
[6] O. Andreikiv, O. Serhienko, et al., Acoustic-emission criteria for rapid analysis of internal defects in composite materials, Mater. Sci. 37 (1) (2001) 106–117.
[7] M. Takemoto, H. Nishino, K. Ono, Wavelet transform-applications to AE signal analysis, Acoust. Emission-beyond the Millenn. (2000) 35–56.
[8] C.U. Grosse, M. Ohtsu, Acoustic Emission Testing, Springer Science & Business Media, 2008.
[9] O.-L. Ouabi, P. Pomarede, M. Geist, N.F. Declercq, C. Pradalier, A FastSLAM approach integrating beamforming maps for ultrasound-based robotic inspection of metal structures, IEEE Robot. Autom. Lett. 6 (2) (2021) 2908–2913.
[10] A. Miranda, J.V. Hook, C. Schaal, Lamb wave-based mapping of plate structures via frontier exploration, Ultrasonics 110 (2021) 106282, http://dx.doi.org/10.1016/j.ultras.2020.106282.
[11] C. Schaal, A. Mal, Lamb wave propagation in a plate with step discontinuities, Wave Motion 66 (2016) 177–189, http://dx.doi.org/10.1016/j.wavemoti.2016.06.012.
[12] Z. Su, L. Ye, Y. Lu, Guided lamb waves for identification of damage in composite structures: A review, J. Sound Vib. 295 (3–5) (2006) 753–780.
[13] M. Alwan, P.J. Rajendran, S. Kell, D. Mack, S. Dalal, M. Wolfe, R. Felder, A smart and passive floor-vibration based fall detector for elderly, in: Information and Communication Technologies, 2006. ICTTA'06. 2nd, 1, IEEE, 2006, pp. 1003–1007.
[14] X. Yu, Approaches and principles of fall detection for elderly and patient, in: E-Health Networking, Applications and Services, 2008. HealthCom 2008. 10th International Conference on, IEEE, 2008, pp. 42–47.
[15] Y. Zigel, D. Litvak, I. Gannot, A method for automatic fall detection of elderly people using floor vibrations and sound—Proof of concept on human mimicking doll falls, IEEE Trans. Biomed. Eng. 56 (12) (2009) 2858–2867.
[16] R. Madarshahian, J.M. Caicedo, D.A. Zambrana, Evaluation of a time reversal method with dynamic time warping matching function for human fall DetectionUsing structural vibrations, in: Model Validation and Uncertainty Quantification, vol. 3, Springer International Publishing, 2014, pp. 171–176.
[17] A.R.O. Lasprilla, J.M. Caicedo, G.A. Ospina, Modeling human–structure interaction using a close loop control system, in: Dynamics of Civil Structures, vol. 4, Springer International Publishing, 2014, pp. 101–108.
[18] V. Hirth, J. Caicedo, S. Langevin, P. Zichl, D. Krotish, FREES: Fall Reduction in the Elderly using Electronic Sensors, J. Am. Geriatr. Soc. 58 (2010) 71.
[19] M. Mirshekari, S. Pan, A. Bannis, Y.P.M. Lam, P. Zhang, H.Y. Noh, Step-level person localization through sparse sensing of structural vibration, in: Proceedings of the 14th International Conference on Information Processing in Sensor Networks, ACM, 2015, pp. 376–377.
[20] M. Lam, M. Mirshekari, S. Pan, P. Zhang, H.Y. Noh, Robust occupant detection through step-induced floor vibration by incorporating structural characteristics, in: Dynamics of Coupled Structures, vol. 4, Springer International Publishing, 2016, pp. 357–367.
[21] S. Pan, M. Mirshekari, P. Zhang, H.Y. Noh, Occupant traffic estimation through structural vibration sensing, in: SPIE Smart Structures and Materials+ Nondestructive Evaluation and Health Monitoring, International Society for Optics and Photonics, 2016, p. 980306.
[22] M. Mirshekari, S. Pan, P. Zhang, H.Y. Noh, Characterizing wave propagation to improve indoor step-level person localization using floor vibration, in: SPIE Smart Structures and Materials+ Nondestructive Evaluation and Health Monitoring, International Society for Optics and Photonics, 2016, p. 980305.
[23] F. Au, R. Jiang, Y. Cheung, Parameter identification of vehicles moving on continuous bridges, J. Sound Vib. 269 (1) (2004) 91–111.
[24] T.H. Chan, L. Yu, S. Law, T. Yung, Moving force identification studies, I: theory, J. Sound Vib. 247 (1) (2001) 59–76.
[25] S. Law, T.H. Chan, Q. Zeng, Moving force identification: a time domain method, J. Sound Vib. 201 (1) (1997) 1–22.
[26] T.H. Chan, S. Law, T. Yung, X. Yuan, An interpretive method for moving force identification, J. Sound Vib. 219 (3) (1999) 503–524.
[27] R. Jiang, F. Au, Y. Cheung, Identification of masses moving on multi-span beams based on a genetic algorithm, Comput. Struct. 81 (22) (2003) 2137–2148.
[28] I.G. Raftoyiannis, T.P. Avraam, G.T. Michaltsos, Analytical models of floating bridges under moving loads, Eng. Struct. 68 (2014) 144–154, http://dx.doi.org/10.1016/j.engstruct.2014.03.002, URL: https://www.sciencedirect.com/science/article/pii/S0141029614001400.

[29] R.T. Corrêa, F. Simões, A.P. da Costa, Moving loads on beams on Winkler foundations with passive frictional damping devices, Eng. Struct. 152 (2017) 211–225, http://dx.doi.org/10.1016/j.engstruct.2017.09.023, URL: https://www.sciencedirect.com/science/article/pii/S0141029617300639.

[30] D.-S. Yang, C. Wang, Dynamic response and stability of an inclined Euler beam under a moving vertical concentrated load, Eng. Struct. 186 (2019) 243–254, http://dx.doi.org/10.1016/j.engstruct.2019.01.140, URL: https://www.sciencedirect.com/science/article/pii/S0141029618325756.

[31] A. Zangeneh, P. Museros, C. Pacoste, R. Karoumi, Free vibration of viscoelastically supported beam bridges under moving loads: Closed-form formula for maximum resonant response, Eng. Struct. 244 (2021) 112759, http://dx.doi.org/10.1016/j.engstruct.2021.112759, URL: https://www.sciencedirect.com/science/article/pii/S0141029621009093.

[32] E. Celebi, G. Schmid, Investigation of ground vibrations induced by moving loads, Eng. Struct. 27 (14) (2005) 1981–1998, http://dx.doi.org/10.1016/j.engstruct.2005.05.011, URL: https://www.sciencedirect.com/science/article/pii/S0141029605002324.

[33] J.-J. Wu, Vibration analyses of an inclined flat plate subjected to moving loads, J. Sound Vib. 299 (1) (2007) 373–387, http://dx.doi.org/10.1016/j.jsv.2006.07.002, URL: https://www.sciencedirect.com/science/article/pii/S0022460X06005621.

[34] L. Ma, H. Ouyang, C. Sun, R. Zhao, L. Wang, A curved 2.5D model for simulating dynamic responses of coupled track-tunnel-soil system in curved section due to moving loads, J. Sound Vib. 451 (2019) 1–31, http://dx.doi.org/10.1016/j.jsv.2019.02.044, URL: https://www.sciencedirect.com/science/article/pii/S0022460X1930152X.

[35] L. Ma, C. Zhang, H. Ouyang, Q. Yan, W. Yu, 2.5D modelling of wave propagation in longitudinally curved viscoelastic structure using a coupled FEM-PML approach, Eng. Struct. 226 (2021) 111337, http://dx.doi.org/10.1016/j.engstruct.2020.111337, URL: https://www.sciencedirect.com/science/article/pii/S0141029620339389.

[36] A. Fathi, B. Poursartip, L.F. Kallivokas, Time-domain hybrid formulations for wave simulations in three-dimensional PML-truncated heterogeneous media, Internat. J. Numer. Methods Engrg. 101 (3) (2015) 165–198.

[37] S. Kucukcoban, L.F. Kallivokas, Mixed perfectly-matched-layers for direct transient analysis in 2D elastic heterogeneous media, Comput. Methods Appl. Mech. Engrg. 200 (2011) 57–76.

[38] C. Jeong, A.C.S. Peixoto, A. Aquino, S. Lloyd, S. Arhin, Genetic algorithm-based acoustic-source inversion approach to detect multiple moving wave sources of an arbitrary number, J. Comput. Civ. Eng. 31 (5) (2017) 04017020.

[39] Q. Mei, M. Gül, M. Boay, Indirect health monitoring of bridges using Mel-frequency cepstral coefficients and principal component analysis, Mech. Syst. Signal Process. 119 (2019) 523–546, http://dx.doi.org/10.1016/j.ymssp.2018.10.006, URL: http://www.sciencedirect.com/science/article/pii/S0888327018306678.

[40] B. Guidio, C. Jeong, On the feasibility of simultaneous identification of a material property of a Timoshenko beam and a moving vibration source, Eng. Struct. 227 (2021) 111346, http://dx.doi.org/10.1016/j.engstruct.2020.111346.

[41] F. Lloyd, C. Jeong, Adjoint equation-based inverse-source modeling to reconstruct moving acoustic sources in a 1D heterogeneous solid, J. Eng. Mech. 144 (9) (2018) 04018089, http://dx.doi.org/10.1061/(ASCE)EM.1943-7889.0001508.

[42] S. Lloyd, C. Jeong, Identifying moving vibrational sources in a truncated, damped, heterogeneous solid, Int. J. Comput. Methods (2022) http://dx.doi.org/10.1142/S021987622250030X, (accepted).

[43] R.L. Taylor, FEAP–A finite element analysis program, 2003.

[44] B. Guidio, B. Jeremić, L. Guidio, C. Jeong, Passive seismic inversion of SH wave input motions in a truncated domain, Soil Dyn. Earthq. Eng. 158 (2022) 107263, http://dx.doi.org/10.1016/j.soildyn.2022.107263, URL: https://www.sciencedirect.com/science/article/pii/S0267726122001129.

[45] D. Komatitsch, J. Tromp, Introduction to the spectral element method for three-dimensional seismic wave propagation, Geophys. J. Int. 139 (3) (1999) 806–822.

[46] D. Komatitsch, S. Tsuboi, J. Tromp, The spectral-element method in seismology, Seismic Earth: Array Analysis of Broadband Seismograms (2005) 205–227.

[47] D. Komatitsch, J. Ritsema, J. Tromp, The spectral-element method, Beowulf computing, and global seismology, Science 298 (5599) (2002) 1737–1742.

[48] J. Tromp, D. Komattisch, Q. Liu, Spectral-element and adjoint methods in seismology, Commun. Comput. Phys. 3 (1) (2008) 1–32.